National Aeronautics and
Space Administration

Dryden Flight Research Center
P.O. Box 273
Edwards, California 93523-0273

Reply to
Attn of: F-1998-02-D-1048 January 22, 1998

TO: All Holders of NASA/TM-97-206318, Dated December 1997

FROM: F/Technical Publications Office

SUBJECT: Errata Sheet for NASA/TM-97-206318, Dated December 1997

NASA/TM-97-206318, *Linearized Poststall Aerodynamic and Control Law Models of the X-31A Aircraft and Comparison With Flight Data*, by P. C. Stoliker, John T. Bosworth, and Jennifer Georgie has an error in equation (3) and equation (5) on page 9. Please make the following changes to this document.

1. Delete the current text on page 9 and 10.
2. Insert the new attached page 9 and 10 with the corrected equations (3) and (5).
3. Staple the errata sheet to the inside front cover of the document.

Thank you for your cooperation.

Camilla F. McArthur
Administrative Operations Specialist

Attachment
as stated

NASA/TM-97-206318

Linearized Poststall Aerodynamic and Control Law Models of the X-31A Aircraft and ComparisonWith Flight Data

P. C. Stoliker, John T. Bosworth, and Jennifer Georgie
Dryden Flight Research Center
Edwards, California

December 1997

The NASA STI Program Office . . . in Profile

Since its founding, NASA has been dedicated to the advancement of aeronautics and space science. The NASA Scientific and Technical Information (STI) Program Office plays a key part in helping NASA maintain this important role.

The NASA STI Program Office is operated by Langley Research Center, the lead center for NASA's scientific and technical information. The NASA STI Program Office provides access to the NASA STI Database, the largest collection of aeronautical and space science STI in the world. The Program Office is also NASA's institutional mechanism for disseminating the results of its research and development activities. These results are published by NASA in the NASA STI Report Series, which includes the following report types:

- TECHNICAL PUBLICATION. Reports of completed research or a major significant phase of research that present the results of NASA programs and include extensive data or theoretical analysis. Includes compilations of significant scientific and technical data and information deemed to be of continuing reference value. NASA's counterpart of peer-reviewed formal professional papers but has less stringent limitations on manuscript length and extent of graphic presentations.

- TECHNICAL MEMORANDUM. Scientific and technical findings that are preliminary or of specialized interest, e.g., quick release reports, working papers, and bibliographies that contain minimal annotation. Does not contain extensive analysis.

- CONTRACTOR REPORT. Scientific and technical findings by NASA-sponsored contractors and grantees.

- CONFERENCE PUBLICATION. Collected papers from scientific and technical conferences, symposia, seminars, or other meetings sponsored or cosponsored by NASA.

- SPECIAL PUBLICATION. Scientific, technical, or historical information from NASA programs, projects, and mission, often concerned with subjects having substantial public interest.

- TECHNICAL TRANSLATION. English-language translations of foreign scientific and technical material pertinent to NASA's mission.

Specialized services that complement the STI Program Office's diverse offerings include creating custom thesauri, building customized databases, organizing and publishing research results . . . even providing videos.

For more information about the NASA STI Program Office, see the following:

- Access the NASA STI Program Home Page at ***http://www.sti.nasa.gov***

- E-mail your question via the Internet to help@sti.nasa.gov

- Fax your question to the NASA Access Help Desk at (301) 621-0134

- Telephone the NASA Access Help Desk at (301) 621-0390

- Write to:
  NASA Access Help Desk
  NASA Center for AeroSpace Information
  800 Elkridge Landing Road
  Linthicum Heights, MD 21090-2934

NASA/TM-97-206318

Linearized Poststall Aerodynamic and Control Law Models of the X-31A Aircraft and ComparisonWith Flight Data

P. C. Stoliker, John T. Bosworth, and Jennifer Georgie
Dryden Flight Research Center
Edwards, California

National Aeronautics and
Space Administration

Dryden Flight Research Center
Edwards, California 93523-0273

December 1997

NOTICE

Use of trade names or names of manufacturers in this document does not constitute an official endorsement of such products or manufacturers, either expressed or implied, by the National Aeronautics and Space Administration.

Available from:

NASA Center for AeroSpace Information
800 Elkridge Landing Road
Linthicum Heights, MD 21090-2934
Price Code: A16

National Technical Information Service
5285 Port Royal Road
Springfield, VA 22161
Price Code: A16

ABSTRACT

The X-31A aircraft has a unique configuration that uses thrust-vector vanes and aerodynamic control effectors to provide an operating envelope to a maximum 70° angle of attack, an inherently nonlinear portion of the flight envelope. This report presents linearized versions of the X-31A longitudinal and lateral-directional control systems, with aerodynamic models sufficient to evaluate characteristics in the poststall envelope at 30°, 45°, and 60° angle of attack. The models are presented with detail sufficient to allow the reader to reproduce the linear results or perform independent control studies. Comparisons between the responses of the linear models and flight data are presented in the time and frequency domains to demonstrate the strengths and weaknesses of the ability to predict high-angle-of-attack flight dynamics using linear models. The X-31A six-degree-of-freedom simulation contains a program that calculates linear perturbation models throughout the X-31A flight envelope. The models include aerodynamics and flight control system dynamics that are used for stability, controllability, and handling qualities analysis. The models presented in this report demonstrate the ability to provide reasonable linear representations in the poststall flight regime.

NOMENCLATURE

Acronyms

HARV	High Alpha Research Vehicle
MATV	Multi-Axis Thrust Vectoring
TEF	trailing-edge flaps

Symbols

A	state derivative matrix
ALFC	filtered angle-of-attack command, deg
ALFC0	delayed angle-of-attack command, deg
ALFX	processed angle-of-attack feedback, deg
B	control derivative matrix
BETC	commanded angle of sideslip, deg
BETX	processed angle of sideslip, deg
C	state observation matrix
CALFX	cosine of *ALFX*
D	control observation matrix
DAFB	summation of feedback compensation to differential trailing-edge flaps, deg
DALF	feedback error between commanded and sensed angle of attack, deg
DBET	error between commanded and sensed angle of sideslip, deg
DBETDXR	sideslip command from rudder pedals, deg

DDEFC	commanded differential trailing-edge flap deflection, deg
DECAN	canard deflection, deg
DECANC	commanded canard deflection, deg
DECAN_IL	inner-loop feedback to canard, deg
DERUDC	commanded rudder deflection, deg
DEVQ	pitch thrust-vector deflection, deg
DEVQCL	pitch thrust-vector deflection command, deg
DEVR	yaw thrust-vector deflection, deg
DEVRCL	yaw thrust-vector deflection command, deg
DPE	error between stability-axis roll rate and command, deg/sec
DQE	error between flightpath pitch rate and command, deg/sec
DRE	error between stability-axis yaw rate and command, deg/sec
DRFB	summation of feedback compensation to rudder, deg
DRPF	normalized rudder command from flight data
DRUD	rudder deflection, deg
DTED	differential trailing-edge deflection, deg
DTES	symmetric trailing-edge deflection, deg
DTES_IL	inner-loop feedback to trailing-edge flaps, deg
DTESC	commanded symmetric trailing-edge flap deflection, deg
DTR	$\pi/180$, rad/deg
FDWGT0	ratio of estimated thrust to estimated weight
FDWGTINV	inverse of FDWGT0
FFCOMP	angle-of-attack feedforward compensation, deg
FKAPPA	rudder to thrust-vectoring effectiveness multiplier
FZETA	rudder fade multiplier
g	gravitational acceleration constant, 32.2 ft/ sec^2
G0DVK	gravitational acceleration constant divided by velocity, deg/sec
HIAL0	angle-of-attack command to canard gain, deg/deg
HRKBE0	side force for each angle-of-sideslip ratio, *g*/deg
HURBE0	angle-of-sideslip command–to–rudder gain, deg/deg
HURPK0	roll-rate command normalized by velocity–to–rudder gain, ft
HURPP0	roll acceleration–to–rudder gain, deg/(deg/sec^2)
HURRP0	yaw acceleration–to–rudder gain, deg/(deg/sec^2)
HXIBE0	angle-of-sideslip command–to–aileron gain, deg/deg

HXIPK0	roll-rate command normalized by velocity–to–aileron gain, ft
HXIPP0	roll acceleration–to–aileron gain, deg/(deg/sec^2)
HXIRP0	yaw acceleration–to–aileron gain, deg/(deg/sec^2)
I_{xx}	moment of inertia about the x axis, slug-ft^2
I_{xz}	xz product of inertia, slug-ft^2
I_{yy}	moment of inertia about the y axis, slug-ft^2
I_{zz}	moment of inertia about the z axis, slug-ft^2
KADE0	angle of attack–to–trailing-edge flap gain, deg/deg
KBKA0	angle of sideslip–to–thrust-vectoring gain, deg/deg
KBXI0	angle of sideslip–to–aileron gain, deg/deg
KBZE0	angle of sideslip–to–rudder gain, deg/deg
KDEC0	multiplier for ratio of canard from trailing-edge flaps, deg/deg
KDEVQ0	pitch thrust-vectoring gain, deg/deg
KPKKA	roll rate–to–thrust-vectoring gain, deg/(deg/sec)
KPKXI	roll rate–to–aileron gain, deg/(deg/sec)
KPKZE	roll rate–to–rudder gain, deg/(deg/sec)
KQDE0	pitch rate–to–trailing-edge flap gain, deg/(deg/sec)
KRKKA	yaw rate–to–thrust-vector gain, deg/(deg/sec)
KRKXI	yaw rate–to–aileron gain, deg/(deg/sec)
KRKZE	yaw rate–to–rudder gain, deg/(deg/sec)
KXI00	multiplier for ratio of thrust vectoring to aileron, deg/deg
KZETA	thrust vectoring–to–aileron multiplier, deg/deg
m	mass, slug
MSALFX	negative sine of *ALFX*
n_L	stability-axis acceleration, *g*
n_{xcg}	longitudinal acceleration at the center of gravity, *g*
n_{xinu}	longitudinal acceleration at the sensor location, *g*
NXS	sensed body-axis longitudinal acceleration, *g*
n_{ycg}	lateral acceleration at the center of gravity, *g*
n_{yinu}	lateral acceleration at the sensor location, *g*
NYKC	commanded lateral acceleration, *g*
n_{zcg}	normal acceleration at the center of gravity, *g*
NZC	body-axis normal acceleration command, *g*
n_{zinu}	normal acceleration at the sensor location, *g*

NZKC	commanded stability-axis normal acceleration, *g*
NZ30D	computed normal acceleration at 30° angle of attack, *g*
p	body-axis roll rate, deg/sec
PDT	derived roll acceleration, deg/sec^2
PDTFB	feedforward compensation for the lateral axis, deg
PHIF	filtered bank angle, rad
PKC	stability-axis roll-rate command, deg/sec
PKCDVK	roll-rate command normalized by velocity, deg/ft
PKCF	pilot roll-rate command, deg/sec
PKCMAX	maximum stability-axis roll-rate command, deg/sec
p_{stab}	stability-axis roll rate, deg/sec
PS	sensed body-axis roll rate, deg/sec
PSTAB	stability-axis roll rate, deg/sec
q	body-axis pitch rate, deg/sec
Q	pitch rate, deg/sec
QBWGT0	normalized dynamic pressure
QEC	flightpath pitch-rate command, deg/sec
QS	sensed body-axis pitch rate, deg/sec
r	body-axis yaw rate, deg/sec
RDT	derived yaw acceleration, deg/sec^2
RDTFB	feedforward compensation for the directional axis, deg
REC	commanded stability-axis yaw rate, deg/sec
r_{stab}	stability-axis yaw rate, deg/sec
RS	sensed body-axis yaw rate, deg/sec
RSTAB	stability-axis yaw rate, deg/sec
s	Laplace transform variable
SALFX	sine of *ALFX*
T	flight control computer frame rate, 0.02 sec
TCNREF	reference aerodynamic normal force curve
TDECCRU	canard pitch trim, deg
TDETA	pitch trim, deg
TIME	time reference for pilot inputs to simulation, sec
TSDQBDY	dynamic pressure ratio

TVFAC1	thrust-vectoring fade multiplier for lateral-directional axes
TVFAC2	thrust-vectoring fade multiplier for the longitudinal axis
TVFAD	thrust-vectoring engagement multiplier
TVFB	summation of feedback compensation to yaw thrust vectoring, deg
u	control input vector
V	velocity, ft/sec
VINV	inverse of velocity, 1/(ft/sec)
VK0	true airspeed, ft/sec
x	state vector
$\dot{x}$	derivative of the state vector
y	output vector
z	discrete transform variable
α	angle of attack, deg
β	angle of sideslip, deg
γ	flightpath elevation angle, deg
δ_{canard}	canard deflection, deg
δ_{dtef}	differential trailing-edge flap deflection, deg
δ_{lef}	leading-edge flap deflection, deg
δ_{rud}	rudder deflection, deg
δ_{tef}	symmetric trailing-edge flap deflection, deg
δ_{tvvp}	pitch thrust-vector plume deflection, deg
δ_{tvvy}	yaw thrust-vector plume deflection, deg
θ	pitch angle, deg
μ	flightpath bank angle, deg
π	constant, 3.141592654
ϕ	bank angle, deg

Sign Conventions

Angle of attack	Positive noseup
Angle of sideslip	Positive nose left
Canard deflection	Positive trailing-edge down
Differential flap	Positive right trailing-edge down (right – left)/2.0
Lateral acceleration	Positive out right wing

Lateral stick	Positive right roll
Pitch rate	Positive noseup
Pitch stick	Positive aft (noseup command)
Pitch thrust-vector command	Positive nosedown
Roll rate	Positive right wing down
Rudder surface	Positive trailing-edge left
Symmetric flap	Positive trailing-edge down
Yaw rate	Positive nose right
Yaw thrust-vector command	Positive nose left

INTRODUCTION

Regardless of the flight regime to be explored, linear and nonlinear simulations have been used as tools in the design and test processes. Nonlinear simulations, including piloted simulations, have long been used for flight control system checkout, verification and validation of operational flight software, test mission planning, and pilot training. Linear models (which include the flight control system, rigid-body aerodynamics, actuator dynamics, feedback sensors, and filters) have proven to be an invaluable tool for the analysis of new or modified flight control systems, whether the control system design is performed using classical root-locus methods or modern control theories. Linear simulations also provide a cost-effective and timely tool for obtaining surveys of stability, control, and handling qualities characteristics throughout the flight envelope. These models have an important role in the early stages of control system development or control law revisions and have been shown to be valuable when validated against flight test data.[1]

As control system and computer capabilities have advanced, aircraft have continually entered new flight regimes and the necessity for evaluation of linear models has continued. The latest generation of developmental or experimental aircraft has initiated the investigation of controlled flight beyond the stall angle of attack for the wing, or the poststall regime. The capability for sustained and controlled flight in this regime has been provided by integrating multiaxis thrust vectoring into the control laws[2] for the X-31A aircraft, the F-18 High Alpha Research Vehicle (HARV), and the F-16 Multi-Axis Thrust Vectoring (MATV) aircraft. Thrust vectoring has also been demonstrated with two-dimensional converging nozzles for the YF-22 aircraft[3] and the F-15 Short Takeoff and Landing Demonstrator.[4] Initial applications on the F-18 HARV and X-31A aircraft used high-temperature nickel-based steel and carbon-carbon paddles, respectively, to deflect the thrust-vector plume. Recently, rapid advances in engine technology have allowed the incorporation of axisymmetric thrust vectoring into production engines with little or no penalties in aircraft weight or systems.

The X-31A aircraft is a recent example of a poststall-capable aircraft using a “first generation” thrust-vectoring capability. The vehicle is stabilized and controlled by a full authority, fly-by-wire control system that has integrated pitch and yaw thrust vectoring with the aerodynamic control surfaces. Linear models were used extensively in the initial control system design,[5] where a linear quadratic regulator nonzero set-point tracker methodology was used. During flight tests, parameter identification results were used to modify the aerodynamic database.[6] Linear models generated from the modified aerodynamic data

were used to develop control system modification that allowed envelope expansion to proceed to 70° angle of attack and 265 kn poststall entry speed. Subsequent efforts used the linear models for an in-flight simulation of an aircraft with reduced vertical tail size[7] and a high-angle-of-attack handling qualities investigation.[8]

This paper discusses the linear models and validation of the models with flight data for the X-31A aircraft. Three flight conditions have been selected for presentation. These flight conditions provide the ability to examine 1-*g* flight at 30°, 45°, and 60° angle of attack for both the longitudinal and lateral-directional axes. These cases provide a representative sampling of the poststall flight envelope. The rigid-body aerodynamics are calculated using linear perturbation methods of the wind-tunnel and parameter-estimation-modified data six-degree-of-freedom base. The linear models are compared with flight test data in the time and frequency domains.

AIRCRAFT DESCRIPTION

Two X-31A aircraft were built by Rockwell International (Downey, California) and Daimler-Benz Aerospace (Germany) using joint funding from the Advanced Research Projects Agency and Germany's Federal Ministry of Defense. The aircraft (fig. 1) is a single-seat fighter configuration with an empty weight of approximately 12,000 lbm that uses a single GE-F404-400 engine (General Electric, Lynn, Massachusetts). The wing planform is a double-delta with an inboard leading-edge sweep of 56.6° and an outboard sweep of 45°. The wing area, span, and mean chord are 226.3 ft^2, 22.833 ft, and 12.35 ft, respectively. Figure 2 shows an aircraft three-view drawing. Tables 1 and 2 show the physical characteristics and accelerometer locations for the aircraft. A more detailed aircraft description has previously been published.[8]

Four trailing-edge flaps on the wing can be deflected symmetrically for pitch control and differentially (left and right side) for roll control. The inboard and outboard trailing-edge flaps are geared together on each side of the aircraft. The leading-edge flaps are scheduled to deflect symmetrically as a function of angle of attack. An all-moving canard was added to meet the desired instability level for maneuverability and to meet the requirement for aerodynamic recovery from extreme angles of attack. The vertical tail contains a rudder for directional control at less than 40° angle of attack. Pitch and yaw moments can be generated by the three thrust-vector vanes (fig. 3). Table 3 shows the control surface characteristics. The engine inlet lip is moveable and is deflected as a function of angle of attack.

Table 1. Physical characteristics of the X-31A aircraft.

Wing span	22.833 ft
Wing area	226.3 ft^2
Wing leading-edge sweep:	
inboard	56.6 deg
outboard	45 deg
Mean aerodynamic chord	12.35 ft
Vehicle empty weight	12,168 lbm
Maximum fuel capacity	4,000 lbm
Canard area	23.6 ft^2

Table 2. Accelerometer locations of the X-31A aircraft.

Accelerometer	Fuselage station, in.	Buttock line, in.	Waterline, in.
Normal	191.625	5.225	111.672
Lateral	191.625	5.550	111.672
Axial	198.680	5.550	111.672

Table 3. Control surface characteristics.

Control surface	Position limit, deg	Rate limit, deg/sec
Canard	–70, 20	±60
Inboard leading-edge flaps	–40, 0	±25
Outboard leading-edge flaps	–32, 0	±25
Trailing-edge flaps	±30	±60 or ±80*
Rudder	±30	±80
Thrust-vectoring vanes	–48, 35	±60**

*Higher rate allowed for higher engine power settings.

**Paddle-rate limit results in approximately 40 deg/sec plume deflection–rate limit. Paddle limit allowed ±15° plume deflection.

RIGID-BODY AERODYNAMIC MODEL DESCRIPTION

Linear rigid-body aerodynamic models were obtained by solving for steady-state trim points and using finite differences to generate the linear equations of motion. The trim condition was determined by using an iterative search technique to determine deflections of the aerodynamic and thrust control effectors, angle of attack, pitch angle, and thrust to obtain steady-state flight at the desired condition. For each combination of effector position, angle of attack, and thrust, the forces and moments were computed using the full six-degree-of-freedom nonlinear equations of motion with a full envelope aerodynamic database. The aerodynamic database used in the simulation incorporated modifications to the wind-tunnel data using increments calculated using parameter estimation techniques and flight data.[6]

The linear perturbation equations of motion were formulated in the following state space form:

$$\dot{x} = Ax + Bu \tag{1}$$

$$y = Cx + Du \tag{2}$$

The coefficients in the matrices were obtained using a linearization technique that calculates numerical perturbations about the trim condition. The perturbations were ±1 ft/sec for velocity, ±1° for angles of attack and sideslip, ±1 deg/sec for body rates, ±1° for attitudes, and ±1° for control-effector deflections.

Because of the lack of significant cross terms, the linear equations were decoupled for longitudinal and lateral-directional axes. For the longitudinal axis, the vectors x, u, and y are defined as follows:

$$x = [q\ \alpha\ V\ \theta]' \tag{3}$$

$$u = [\delta_{tef}\ \delta_{canard}\ \delta_{lef}\ \delta_{tvvp}]' \tag{4}$$

$$y = [q\ \alpha\ V\ \theta\ n_{zcg}\ n_{zinu}\ n_{xcg}\ n_{xinu}]' \tag{5}$$

For the lateral-directional equations, the vectors x, u and y are defined as follows:

$$x = [p\ r\ \beta\ \phi]' \tag{6}$$

$$u = [\delta_{dtef}\ \delta_{rud}\ \delta_{tvvy}]' \tag{7}$$

$$y = [p\ r\ \beta\ \phi\ n_{ycg}\ n_{yinu}]' \tag{8}$$

FLIGHT CONTROL SYSTEM DESCRIPTION

The X-31A aircraft has a triplex digital flight control system with a fourth computer used as a tie-breaker. The control laws are updated at a rate of 50 samples/sec (the flight control computer frame rate is equal to 0.02 sec). The flight control system provides the capability for the aircraft to demonstrate enhanced fighter maneuverability, especially in the poststall flight regime. The increased maneuverability is obtained through the integration of thrust-vector control paddles with conventional aerodynamic control surfaces.

This section presents the dynamic elements of the flight control system that were included in the linear models. Nonlinear elements such as dead bands, rate limits, and position limits were not included in the linear model and, therefore, are not discussed here. Sensor models and actuator models are included. Computational time delays, as measured on test benches, are also included. The control system gains were calculated using a nonzero set-point tracker linear quadratic regulator method. A more complete description of the flight control system design has previously been published.[5]

Longitudinal Control System

Figure 4 shows a block diagram of the longitudinal linear model of the X-31A control laws. The longitudinal stick input is scaled and translated into a filtered angle-of-attack command, *ALFC*. The *ALFC* is the control input to the feedback compensation and is also fed forward through a lag filter to provide steady-state trim surface-position commands to the canards and symmetric trailing-edge flaps. Figure 5 shows the feedback compensation block diagram.

Processed angle-of-attack feedback (*ALFX*) calculation emulates the blending of inertially calculated quantities with the flow angles from the flight test noseboom (fig. 6). The *ALFC* is subtracted from the *ALFX* to produce a feedback error between commanded and sensed angle of attack, *DALF*. This error is passed through proportional and integral paths to generate surface commands. In addition to the *DALF*, an error between flightpath pitch rate and command, *DQE*, is also used. Filtering for the pitch-rate feedback includes a structural notch filter and a lead-lag filter for phase advance (fig. 7).

The following stability-axis normal acceleration equation is used to derive a flightpath pitch-rate command:[5]

$$n_{zcg} = q * (V/g) * (\pi/180) + \cos(\mu) * \cos(\gamma) \tag{9}$$

where n_{zcg} is the normal acceleration at the center of gravity, q is the body-axis pitch rate, V is the velocity, g is the gravitational acceleration constant, μ is the flightpath bank angle, and γ is the flightpath elevation angle.

Rearranging terms in the equation results in the following:

$$q = (n_{zcg} - \cos(\mu) * \cos(\gamma)) * (g/V) * (180/\pi) \tag{10}$$

By linearizing the gravity term, as expressed by the flightpath angles, the equation simplifies to:

$$q = (n_{zcg} * (g/V)) * (180/\pi) \tag{11}$$

The following derivation shows how the acceleration at the center of gravity is replaced by the commanded acceleration yielding the pitch-rate command required for a maneuver. Stability-axis acceleration, n_L, can be calculated using the following relationship:

$$n_L = n_{zcg} * \cos(\alpha) - n_{xcg} * \sin(\alpha) \tag{12}$$

The commanded stability-axis normal acceleration, *NZKC*, is obtained by replacing the body-axis acceleration with the desired body-axis acceleration commands. Because the longitudinal control system does not include direct control of the x axis through commands to the engine throttle, the sensed longitudinal acceleration is used rather than a commanded axial acceleration.

In terms of X-31A control system variables, the *NZKC* can be expressed as follows:

$$NZKC = NZC * \cos(ALFX) - NXS * \sin(ALFX) \tag{13}$$

where *NZC* is the body-axis normal acceleration command and *NXS* is the sensed body-axis longitudinal acceleration. The resultant flightpath pitch-rate command is as follows:

$$QEC = NZKC * (g/VK0) * (180/\pi) \tag{14}$$

Figure 8 shows the filtering required by the linear model for *NXS*. The *NZC* is calculated from the *ALFC*, and the aerodynamic normal force characteristics of the X-31A aircraft are found by a table lookup based on flight condition.

The feedback and feedforward commands are combined to generate control surface commands to the canard, symmetric trailing-edge flaps, and the pitch thrust-vector system (figs. 4 and 5). Figures 9 to 11 show the models, including filters, for the canard, trailing-edge flaps and pitch thrust vectoring. The leading-edge flaps are scheduled to deflect as a function of angle of attack and are fully extended for poststall flight. For this reason, the flaps are neglected in the linear models.

Lateral-Directional Control System

Figure 12 shows a block diagram of the lateral-directional linear model of the X-31 control laws. The lateral stick input is scaled by the maximum stability-axis roll-rate command, *PKCMAX*, to the stability-axis roll-rate command, *PKC*. The *PKCMAX* is a function of dynamic pressure, angle of attack, and estimated thrust to ensure that the thrust-vector vanes can generate enough control moment to coordinate a turn. The rudder pedals command the angle of sideslip, which is scaled for the maximum angle-of-sideslip command. The maximum angle-of-sideslip command is a function of true airspeed, angle of attack, and dynamic pressure. The rudder-pedal command authority is faded from 1.0 to 0.0 between 30° and 45° angle of attack. This fade is caused by the loss of rudder effectiveness as angle of attack increases.

The primary feedbacks for the lateral-directional flight control system are the sensed body-axis roll rate, *PS*, sensed body-axis yaw rate, *RS*, and processed angle of sideslip, *BETX*. Bank angle, ϕ, is used for gravity compensation. The *BETX* is obtained from a blended combination of inertial measurements and sideslip from the flight test noseboom flow vane. Figure 13 shows the linear model for this function. Figures 14 to 16 show the filters required for roll rate, yaw rate, and bank angle.

Figure 17 shows the calculations for the feedback parameters and includes the stability-axis transformation for the rates, the gravity compensation, and the generation of the yaw-rate command. Sensed body-axis roll and yaw rate are converted to the stability-axis roll and yaw rate by the following equations:

$$p_{stab} = p * \cos(\alpha) + r * \sin(\alpha) \tag{15}$$

$$r_{stab} = r * \cos(\alpha) - p * \sin(\alpha) \tag{16}$$

Figure 18 shows the implementation of the conversion between body- and stability-axis rates in terms of X-31A control system variables:

$$PSTAB = PS * \cos(ALFX) + RS * \sin(ALFX) \tag{17}$$

$$RSTAB = RS * \cos(ALFX) - PS * \sin(ALFX) \tag{18}$$

The error between stability-axis roll rate and command, *DPE*, is obtained from the difference between the stability-axis roll-rate, *PSTAB*, and *PKC*. Similarly, the error between commanded and sensed angle of sideslip, *DBET*, is obtained from *BETX* and the commanded angle of sideslip, *BETC*. The commanded stability-axis yaw rate, *REC*, is obtained from the following stability-axis lateral acceleration equation:[5]

$$n_{ycg} = r * (V/g) * (\pi/180) - \sin(\mu) * \cos(\gamma) \tag{19}$$

Rearranging terms in the equation results in the following:

$$r = (n_{ycg} + \sin(\mu) * \cos(\gamma)) * (g/V) * (180/\pi) \tag{20}$$

Linearizing the gravity term (as reflected by the flightpath angle terms) reduces to be equal to the bank angle, ϕ:

$$r = (n_{ycg} + \phi) * (g/V) * (180/\pi) \tag{21}$$

The calculation of the yaw-rate command requires the definition of the lateral acceleration command, which can be calculated using the following relationship:

$$n_{ycg} = [(\text{drag} - \text{thrust} * \cos(\alpha)) * \sin(\beta)]/(m * g) \tag{22}$$

This equation represents the contributions of the normalized $(\text{drag}/(m * g))$ and thrust $(\text{thrust}/(m * g))$ components. The normalized drag component is estimated by a table lookup value based on flight condition. Estimated thrust is calculated using flight condition and sensed engine parameters. The equation is simplified by using the small angle approximation for the sine function and replacing the angle of sideslip, β, with the *BETC*. In terms of X-31A control system variables, the commanded lateral acceleration, *NYKC*, can be expressed as follows:

$$NYKC = HRKBE0 * \text{QBWGT0} - \text{FDWGT0} * \cos(ALFX)) * BETC(\pi/180) \tag{23}$$

Thus, the *REC* can be expressed in terms of X-31A control system variables shown in figure 19:

$$REC = (NYKC + \phi) * (g/VK0) * (180/\pi) \tag{24}$$

Angular accelerations caused by the gravity terms are compensated by a feedforward command (fig. 20). The gravity contribution is differentiated and transformed into the stability axis.

The three feedback error signals (*DPE*, *DRE*, and *DBET*) are passed through a gain compensation (fig. 21). Figure 22 shows forward-path compensation gains. The feedback and feedforward compensation paths are combined to provide commands to the differential trailing-edge flaps, the rudder control surfaces, and the yaw thrust-vector system (fig. 23). Figures 24 to 26 show the filtering and actuator models for the differential trailing-edge flaps, rudder, and yaw thrust vectoring.

SELECTED FLIGHT CONDITIONS FOR LINEAR MODELS

Flight conditions were selected to provide the opportunity to examine the poststall characteristics of the X-31A aircraft and the unique control configuration provided by the addition of thrust vectoring as a control variable. The flight conditions provide a survey of 1-g characteristics at 30°, 45° and 60° angle of attack. Table 4 shows the three longitudinal and three lateral-directional cases presented in this report. Tables 5, 6, and 7 show the trim surface positions, weights, and inertial characteristics for each case.

Table 4. Trim conditions for the six linear models.

Case no.	Target angle of attack, deg	Angle of attack, deg	Altitude, ft	Load factor, *g*	Mach no.	True velocity, ft/sec	Input
1	30	29.9	34,900	0.93	0.373	363	Pitch doublet
2	30	24.8	24,000	1.90	0.435	444	Yaw/roll doublet
3	45	46.1	30,800	0.69	0.270	268	Pitch doublet
4	45	38.4	22,700	1.33	0.326	334	Roll doublet
5	60	59.9	31,600	0.73	0.263	260	Pitch doublet
6	60	59.2	21,300	0.50	0.174	179	Roll doublet

Table 5. Trim surface positions.

Case no.	Canard position, deg	Symmetric flap position, deg
1	–30.9	1.8
2	–23.3	–2.5
3	–39.9	–2.1
4	–35.4	–3.9
5	–42.7	–4.2
6	–40.3	–6.2

Table 6. Mass properties descriptions.

Case no.	Weight, lbm	I_{xx}, slug-ft^2	I_{yy}, slug-ft^2	I_{zz}, slug-ft^2	I_{xz}, slug-ft^2
1	14,500	3,110	35,400	36,200	–224
2	14,100	3,060	35,300	36,100	–209
3	15,000	3,180	35,500	36,300	–242
4	14,200	3,080	35,300	36,100	–214
5	13,600	3,010	35,100	36,000	–192
6	13,600	3,010	35,100	36,000	–192

Table 7. Center-of-gravity locations.

Case no.	Fuselage station, in.	Buttock line, in.	Waterline, in.
1	268.8	0.0	97.4
2	269.6	0.0	97.0
3	269.3	0.0	98.1
4	270.1	0.0	97.1
5	271.0	0.0	96.5
6	272.0	0.0	96.5

State space models are presented for the longitudinal and lateral-directional axes for each of the cases. Tables 8 and 9 show the flight control system gains scheduled as a function of flight condition for all six cases. Tables 10 to 15 show the state space matrices for the linearized airframes.

Table 8. Control system gains for the longitudinal cases.

Gain	Case 1	Case 3	Case 5
CALFX	0.867	0.693	0.501
FDWGTINV	5.560	2.493	2.580
G0DVK	5.077	6.882	7.102
HIAL0	1.020	1.141	1.166
KADE0	1.177	0.781	0.792
KDEC0	–0.758	–1.051	–1.299
KDEVQ0	0.205	0.278	0.299
KQDE0	0.754	0.682	0.672
NZ30D	0.933	0.658	0.619
SALFX	0.498	0.721	0.866
TCNREF	0.016	0.014	0.003
TDECCRU	–1.400	0.000	–0.595
TDETA	–0.037	–0.066	–0.109
TVFAC2	1.017	1.000	1.000
TVFAD	0.976	1.000	1.000

Table 9. Controls system gains and constants for the lateral-directional cases.

Gain	Case 2	Case 4	Case 6
CALFX	0.908	0.783	0.512
DBETDXR	4.385	2.038	0.000
FDWGT0	0.618	0.610	0.592
FDWGTINV	1.619	1.640	1.690
FKAPPA	0.000	0.030	0.016
FZETA	1.000	0.434	0.000
G0DVK	4.147	5.515	10.300
HRKBE0	–12.639	3.026	25.555
HURBE0	0.462	1.955	–6.024
HURPK0	–32.501	–63.611	–36.634
HURPP0	0.125	0.420	–0.411
HURRP0	–2.601	–5.879	–8.630
HXIBE0	–0.852	–2.184	–1.609
HXIPK0	–8.940	28.608	16.141
HXIPP0	–0.218	–0.635	–0.619
HXIRP0	–0.269	–0.104	–0.157
KBKA0	–0.147	–0.759	–0.906
KBXI0	–0.787	–1.171	0.669
KBZE0	–0.997	–0.966	–0.001
KPKKA	0.042	0.190	0.441
KPKXI	0.187	0.787	0.715
KPKZE	0.286	0.256	0.000
KRKKA	0.105	0.530	0.401
KRKXI	0.153	–0.778	–0.936
KRKZE	0.735	0.610	0.000
KXI00	0.080	–0.011	0.001
KZETA	3.405	6.080	0.000
MSALFX	–0.418	–0.622	–0.859
QBWGT0	0.090	0.053	0.016
SALFX	0.418	0.622	0.859
TSDQBDY	0.190	0.322	1.076
TVFAC1	1.000	1.000	1.000
TVFAD	1.000	1.000	1.000
VINV	0.002	0.003	0.006

Table 10. Longitudinal state space matrices for 30° angle of attack.

A Matrix (4 by 4)			
–0.2592E+00	0.1293E+01	0.3081E–01	0.4940E–02
0.1000E+01	–0.6681E–01	–0.2386E–01	0.1689E–01
0.0000E+00	–0.2097E+00	–0.6462E–01	–0.5493E+00
0.1000E+01	0.0000E+00	0.0000E+00	0.0000E+00
B Matrix (4 by 4)			
0.7888E+00	–0.1324E+01	0.1856E–01	–0.1740E+01
–0.1039E–01	–0.4400E–01	0.4200E–02	–0.1806E–01
–0.5900E–02	–0.1619E+00	–0.1480E–01	–0.6571E–01
0.0000E+00	0.0000E+00	0.0000E+00	0.0000E+00
C Matrix (8 by 4)			
0.1000E+01	0.0000E+00	0.0000E+00	0.0000E+00
0.0000E+00	0.1000E+01	0.0000E+00	0.0000E+00
0.0000E+00	0.0000E+00	0.1000E+01	0.0000E+00
0.0000E+00	0.0000E+00	0.0000E+00	0.1000E+01
0.0000E+00	0.1532E–01	0.5000E–02	–0.2000E–04
–0.9100E–03	0.1985E–01	0.5110E–02	0.0000E+00
0.0000E+00	0.5100E–03	0.5600E–03	0.6000E–04
0.2300E–03	–0.3200E–03	0.5400E–03	0.5000E–04
D Matrix (8 by 4)			
0.0000E+00	0.0000E+00	0.0000E+00	0.0000E+00
0.0000E+00	0.0000E+00	0.0000E+00	0.0000E+00
0.0000E+00	0.0000E+00	0.0000E+00	0.0000E+00
0.0000E+00	0.0000E+00	0.0000E+00	0.0000E+00
0.1870E–02	0.1002E–01	–0.4900E–03	0.4100E–02
0.4630E–02	0.5390E–02	–0.4200E–03	–0.1990E–02
0.8600E–03	–0.5000E–04	–0.8100E–03	0.0000E+00
0.3500E–03	0.8100E–03	–0.8200E–03	0.1120E–02

Table 11. Lateral-directional state space matrices for 30° angle of attack.

A Matrix (4 by 4)			
–0.6926E+00	0.7904E+00	–0.3420E+02	0.0000E+00
–0.8387E–01	–0.3457E+00	–0.6763E+00	0.0000E+00
0.4208E+00	–0.9033E+00	–0.1177E+00	0.7172E–01
0.1000E+01	–0.1209E+00	0.0000E+00	–0.1038E–01
B Matrix (4 by 3)			
–0.2471E+02	0.2209E+01	0.1022E+01	
–0.1025E+01	–0.1827E+01	–0.4375E+01	
0.3700E–01	0.3229E–01	0.4497E–01	
0.0000E+00	0.0000E+00	0.0000E+00	
C Matrix (6 by 4)			
0.1000E+01	0.0000E+00	0.0000E+00	0.0000E+00
0.0000E+00	0.1000E+01	0.0000E+00	0.0000E+00
0.0000E+00	0.0000E+00	0.1000E+01	0.0000E+00
0.0000E+00	0.0000E+00	0.0000E+00	0.1000E+01
0.3000E–03	0.1080E–02	–0.2133E–01	–0.4000E–04
–0.1600E–03	0.3300E–03	–0.4653E–01	–0.4000E–04
D Matrix (6 by 3)			
0.0000E+00	0.0000E+00	0.0000E+00	
0.0000E+00	0.0000E+00	0.0000E+00	
0.0000E+00	0.0000E+00	0.0000E+00	
0.0000E+00	0.0000E+00	0.0000E+00	
0.8920E–02	0.7780E–02	0.1084E–01	
–0.1118E–01	0.2800E–02	–0.3930E–02	

Table12. Longitudinal state space matrices for 45° angle of attack.

A Matrix (4 by 4)			
–0.2313E+00	–0.6293E–01	0.3061E–01	0.4640E–02
0.1000E+01	–0.3459E–01	–0.3272E–01	0.1642E–01
0.0000E+00	–0.1472E+00	–0.1059E+00	–0.5546E+00
0.1000E+01	0.0000E+00	0.0000E+00	0.0000E+00
B Matrix (4 by 4)			
0.5252E+00	–0.5492E+00	–0.9660E–02	–0.2894E+01
–0.5730E–02	–0.1339E–01	0.1840E–02	–0.3184E–01
–0.4120E–02	–0.8698E–01	–0.4440E–02	–0.1526E+00
0.0000E+00	0.0000E+00	0.0000E+00	0.0000E+00
C Matrix (8 by 4)			
0.1000E+01	0.0000E+00	0.0000E+00	0.0000E+00
0.0000E+00	0.1000E+01	0.0000E+00	0.0000E+00
0.0000E+00	0.0000E+00	0.1000E+01	0.0000E+00
0.0000E+00	0.0000E+00	0.0000E+00	0.1000E+01
0.0000E+00	0.1024E–01	0.5120E–02	–0.3000E–04
–0.7900E–03	0.1001E–01	0.5230E–02	–0.2000E–04
0.0000E+00	–0.1290E–02	0.5700E–03	0.4000E–04
0.3500E–03	–0.1250E–02	0.5600E–03	0.4000E–04
D Matrix (8 by 4)			
0.0000E+00	0.0000E+00	0.0000E+00	0.0000E+00
0.0000E+00	0.0000E+00	0.0000E+00	0.0000E+00
0.0000E+00	0.0000E+00	0.0000E+00	0.0000E+00
0.0000E+00	0.0000E+00	0.0000E+00	0.0000E+00
0.6700E–03	0.3300E–02	–0.9000E–04	0.6630E–02
0.2520E–02	0.1360E–02	–0.1200E–03	–0.3570E–02
0.5100E–03	–0.4700E–03	–0.2900E–03	0.4000E–04
0.1900E–03	–0.1400E–03	–0.2800E–03	0.1860E–02

Table 13. Lateral-directional state space matrices for 45° angle of attack.

A Matrix (4 by 4)			
0.1630E+01	–0.1356E+01	–0.1070E+02	0.0000E+00
–0.4152E+00	0.3274E+00	0.1938E+01	0.0000E+00
0.6175E+00	–0.7738E+00	–0.7589E–01	0.9599E–01
0.1000E+01	–0.4160E–02	0.0000E+00	–0.2700E–03
B Matrix (4 by 3)			
–0.4571E+01	0.1034E+00	0.9682E+00	
–0.3659E+00	–0.7325E+00	–0.4269E+01	
0.1016E–01	0.1455E–01	0.5786E–01	
0.0000E+00	0.0000E+00	0.0000E+00	
C Matrix (6 by 4)			
0.1000E+01	0.0000E+00	0.0000E+00	0.0000E+00
0.0000E+00	0.1000E+01	0.0000E+00	0.0000E+00
0.0000E+00	0.0000E+00	0.1000E+01	0.0000E+00
0.0000E+00	0.0000E+00	0.0000E+00	0.1000E+01
–0.6400E–03	0.1820E–02	–0.7940E–02	–0.4000E–04
–0.8100E–03	0.2050E–02	–0.8110E–02	–0.4000E–04
D Matrix (6 by 3)			
0.0000E+00	0.0000E+00	0.0000E+00	
0.0000E+00	0.0000E+00	0.0000E+00	
0.0000E+00	0.0000E+00	0.0000E+00	
0.0000E+00	0.0000E+00	0.0000E+00	
0.1840E–02	0.2640E–02	0.1050E–01	
–0.2470E–02	0.1000E–03	–0.4030E–02	

Table 14. Longitudinal state space matrices for 60° angle of attack.

A Matrix (4 by 4)			
–0.1859E+00	–0.7335E–01	0.3132E–01	0.6300E–02
0.1000E+01	–0.2695E–01	–0.2634E–01	0.6718E–01
0.0000E+00	0.3972E–01	–0.1478E+00	–0.4699E+00
0.1000E+01	0.0000E+00	0.0000E+00	0.0000E+00
B Matrix (4 by 4)			
0.6008E+00	–0.3392E+00	–0.4820E–02	–0.2884E+01
–0.5420E–02	–0.5320E–02	0.7700E–03	–0.2617E–01
–0.4770E–01	–0.7037E–01	–0.2840E–02	–0.2022E+00
0.0000E+00	0.0000E+00	0.0000E+00	0.0000E+00
C Matrix (8 by 4)			
0.1000E+01	0.0000E+00	0.0000E+00	0.0000E+00
0.0000E+00	0.1000E+01	0.0000E+00	0.0000E+00
0.0000E+00	0.0000E+00	0.1000E+01	0.0000E+00
0.0000E+00	0.0000E+00	0.0000E+00	0.1000E+01
0.0000E+00	0.1040E–02	0.5660E–02	–0.2000E–04
–0.6600E–03	0.7700E–03	0.5770E–02	0.0000E+00
0.0000E+00	0.1110E–02	0.6100E–03	0.5000E–04
0.2500E–03	0.1160E–02	0.5800E–03	0.4000E–04
D Matrix (8 by 4)			
0.0000E+00	0.0000E+00	0.0000E+00	0.0000E+00
0.0000E+00	0.0000E+00	0.0000E+00	0.0000E+00
0.0000E+00	0.0000E+00	0.0000E+00	0.0000E+00
0.0000E+00	0.0000E+00	0.0000E+00	0.0000E+00
0.1670E–02	0.2270E–02	0.2000E–04	0.7290E–02
0.3830E–02	0.1050E–02	0.0000E+00	–0.3100E–02
–0.8000E–04	–0.4500E–03	–0.1400E–03	0.4000E–04
–0.5000E–03	–0.2200E–03	–0.1300E–03	0.2050E–02

Table 15. Lateral-directional state space matrices for 60° angle of attack.

A Matrix (4 by 4)			
–0.1701E+00	0.2849E+00	–0.3655E+01	0.0000E+00
–0.2376E–01	–0.7870E–02	0.5032E+00	0.0000E+00
0.8575E+00	–0.5142E+00	–0.4192E–01	0.1475E+00
0.1000E+01	0.6898E+00	0.0000E+00	–0.1633E–01
B Matrix (4 by 3)			
–0.1609E+01	0.2000E–04	0.1091E+01	
0.6701E–01	–0.3600E–03	–0.4220E+01	
–0.4490E–02	0.0000E+00	0.1121E+00	
0.0000E+00	0.0000E+00	0.0000E+00	
C Matrix (6 by 4)			
0.1000E+01	0.0000E+00	0.0000E+00	0.0000E+00
0.0000E+00	0.1000E+01	0.0000E+00	0.0000E+00
0.0000E+00	0.0000E+00	0.1000E+01	0.0000E+00
0.0000E+00	0.0000E+00	0.0000E+00	0.1000E+01
–0.9000E–04	–0.1300E–03	0.1190E–02	–0.3000E–04
–0.3800E–03	0.5000E–04	0.5000E–03	–0.3000E–04
D Matrix (6 by 3)			
0.0000E+00	0.0000E+00	0.0000E+00	
0.0000E+00	0.0000E+00	0.0000E+00	
0.0000E+00	0.0000E+00	0.0000E+00	
0.0000E+00	0.0000E+00	0.0000E+00	
–0.4400E–03	0.0000E+00	0.1089E–01	
–0.1300E–02	0.0000E+00	–0.3640E–02	

LINEAR MODEL AND FLIGHT DATA COMPARISONS

Time-domain comparisons are shown in this section for each of the selected flight conditions. Pilot inputs recorded in flight were used as inputs to the simulations to provide the time-domain comparisons. Unfortunately, no frequency sweeps were performed during the X-31A poststall flight testing. The longitudinal pitch doublets, however, provided sufficient excitation to produce reasonable frequency responses when passed through a fast Fourier transformation algorithm. Standard linear methods were used to calculate frequency responses from the linear models for the same flight conditions. Fast Fourier transformation of the roll doublets generally did not provide reasonable results; however, adequate frequency content existed for one case to generate a comparison for the lateral-directional axes at 45° angle of attack.

Longitudinal Comparisons

Pitch doublets were performed at the three selected flight conditions. The *ALFC* was used as input to the linear models. The *ALFC* was measured downstream of the nonlinear elements in the pilot command path. The most noticeable nonlinearity is a 25-deg/sec rate limit imposed by the flight control system on the pilot command. Figures 27 to 29 show the response of the vehicle compared with the response of the linear model to the pitch doublets. For all three cases, the response of the linear models correlates well with the flight-measured responses. For the 45° and 60° angle-of-attack cases, the linear model required less control surface and thrust-vector deflection to achieve the same vehicle motion (fig. 28(b)). Two potential sources exist for the difference: nonlinearities in the aerodynamics or control system, or a difference between the modeled and actual control effectiveness. For example, the linear model uses a control surface effectiveness based on ±1° deflection from the trim point, and surface deflections of larger magnitudes can have a varying effectiveness over the range of deflection.

A comparison between a nonlinear simulation and the flight data for the 45° angle-of-attack case shows good correlation, although a bias exists between the flight and simulation trim deflections (fig. 30). This comparison shows that the linearization process caused the differences shown in figure 28. Further study of the 45° angle-of-attack case shows several reasons for the differences seen in the surface deflections. Figure 31 shows a comparison between the eigenvalues at 40° and 45° angle of attack. At the high angles of attack, the basic airframe longitudinal characteristics change from an unstable divergence to a nearly neutrally damped oscillation over a small change in angle of attack. To account for these changes in dynamics, the flight control system gains are also a strong function of angle of attack. The nonlinear simulation shows how the angle of attack–to–trailing-edge flap gain, *KADE0*, and the pitch rate–to–trailing-edge flap gain, *KQDE0*, vary throughout the maneuver at 45° angle of attack (fig. 30).

The shape of the canard trace (fig. 28) is strongly influenced by the forward path command to the canard. Figure 32 shows the canard position commanded by the forward path. The output of the forward path is a function of the delayed angle-of-attack command, *ALFC0*, which is a nonlinear element. The linear models represent this element by a gain (canard pitch trim, *TDECCRU*), which is the slope of the curve shown in figure 32. As can be seen in figure 32, the slope between 40° and 50° angle of attack is approximately 0.0, and between 35° and 40° angle of attack, the slope is –1.2. The original linear model has a calculated gain of 0.0. Despite these nonlinear characteristics, the linear models provide a reasonable representation of the aircraft response at high angles of attack over the frequency range of interest, 0.3 to 20 rad/sec.

Figures 33 to 38 show the frequency response of the linear models compared to results obtained from fast Fourier transformation of flight-measured data. The responses of pitch rate and angle of attack caused by angle-of-attack command are shown. An unexpected benefit of the rate limiting on the longitudinal pilot command path was that better frequency responses were obtained. The sharp corners introduced by the rate limiting caused a broader range of frequencies to be excited. The comparisons of the frequency responses show that the linear models produce a reasonable representation of the vehicle closed-loop behavior at all angles of attack.

Lateral-Directional Comparisons

Time-domain comparisons were made for roll doublets at the three selected flight conditions. As with the longitudinal axis, the nonlinearities of the stick shaping were avoided by using a measurement of the

shaped pilot *PKC* as input to the linear models. Figures 39 to 41 show the response of the vehicle compared with the response of the linear model to the roll doublets. In general, the time history matches show good correlation with flight-measured responses. The angle-of-sideslip responses do not correlate as well as the other response parameters. The control laws were designed to produce no angle of sideslip during the roll stick input, and the angle-of-sideslip command caused by rudder pedal was reduced to zero at 45° angle of attack and greater. As a result, the angle-of-sideslip excitation caused by the pilot inputs is on the same order of magnitude as the angle of sideslip caused by disturbances. As with the longitudinal doublets, the amount of control surface required to achieve the same vehicle response was not well-predicted by the linear models.

Figure 42 shows the frequency response of the linear model at 45° angle of attack compared to results obtained from fast Fourier transformation of flight-measured data. This case was the only lateral-directional case that had sufficient time at the target angle of attack to extract a frequency response. Although extracting a smooth transfer function from the flight data was not possible, the comparison with the linear model shows reasonable agreement.

CONCLUDING REMARKS

Linear models of the X-31A aircraft have been presented for six poststall flight conditions. Sufficient descriptions of the flight control system and state space representations of the aerodynamics have been included so that the linear models can be reproduced by the reader. The purpose has been to provide validated aerodynamic and control system models for the unique poststall portion of the flight envelope, using thrust vectoring as an additional control effector.

The poststall flight regime is a very nonlinear environment; however, the results and models presented in this report demonstrate that local linearization techniques can be used and do provide a reasonable representation of the airframe and control system. The successful flight results of the X-31A aircraft demonstrate that the use of linear models for control system design is an appropriate strategy for the high-angle-of-attack regime.

Flight data comparisons with the linear models have been presented for the 1-g flight conditions to demonstrate that these models are representative of the flight test vehicle. Comparisons have been made in both the time and frequency domains. In general, the response measurements from flight correlated well with the linear model responses. The surface inputs required to achieve these responses did not correlate as well. The differences observed were mostly attributable to the sensitivity of the aircraft dynamics and control system gains to changes in angle of attack.

The frequency response correlations for the longitudinal axis show surprisingly good agreement, considering that a tailored input such as a frequency sweep was not used. The lateral-axis frequency response comparison demonstrated that the linear model is a reasonable representation of the actual aircraft in flight.

Dryden Flight Research Center
National Aeronautics and Space Administration
Edwards, California, January 23, 1997

REFERENCES

[1]Bosworth, John T., *Linearized Aerodynamic and Control Law Models of the X-29A Airplane and Comparison With Flight Data*, NASA TM-4356, 1992.

[2]Flynn, Billy, Rogers E. Smith, and Ed Schneider, "Thrust Vectoring: A New Dimension," *Canadian Aeronautics and Space Journal*, vol. 41, no. 4, Dec. 1995, pp. 171–178.

[3]Clark, C. and M. Bernens, "High Angle-of-Attack Flight Characteristics of the YF-22," AIAA 91-3194, Sept. 1991.

[4]Bursey, R. and R. Dickinson, "Flight Test Results of the F-15 SMTD Thrust Vectoring/Thrust Reversing Exhaust Nozzle," AIAA 90-1906, July 1990.

[5]Beh, H. and G. Hofinger, "X-31A Control Law Design," *Technologies for Highly Maneuverable Aircraft*, AGARD CP-548, 1994, pp. 13-1–13-9. (Available from DTIC as AD 280 271.)

[6]Weiss, S., D. Rohlf, and E. Plaetschke, "Parameter Identification for X-31A at High Angles of Attack," *Fourth High Alpha Conference*, NASA CP-10143, 1994.

[7]Bosworth, John T. and P. C. Stoliker, *The X-31A Quasi-Tailless Flight Test Results*, NASA TP-3624, 1996.

[8]Stoliker, P. C., *High-Angle-of-Attack Handling Qualities Predictions and Criteria Evaluation for the X-31A*, NASA TM-4758, 1997. (Distribution authorized to U.S. Government agencies and their contractors; other requests shall be referred to WL/FIMS Wright-Paterson AFB, Ohio 45433-6503.)

EC 94 42478-1

Figure 1. X-31A aircraft in poststall flight.

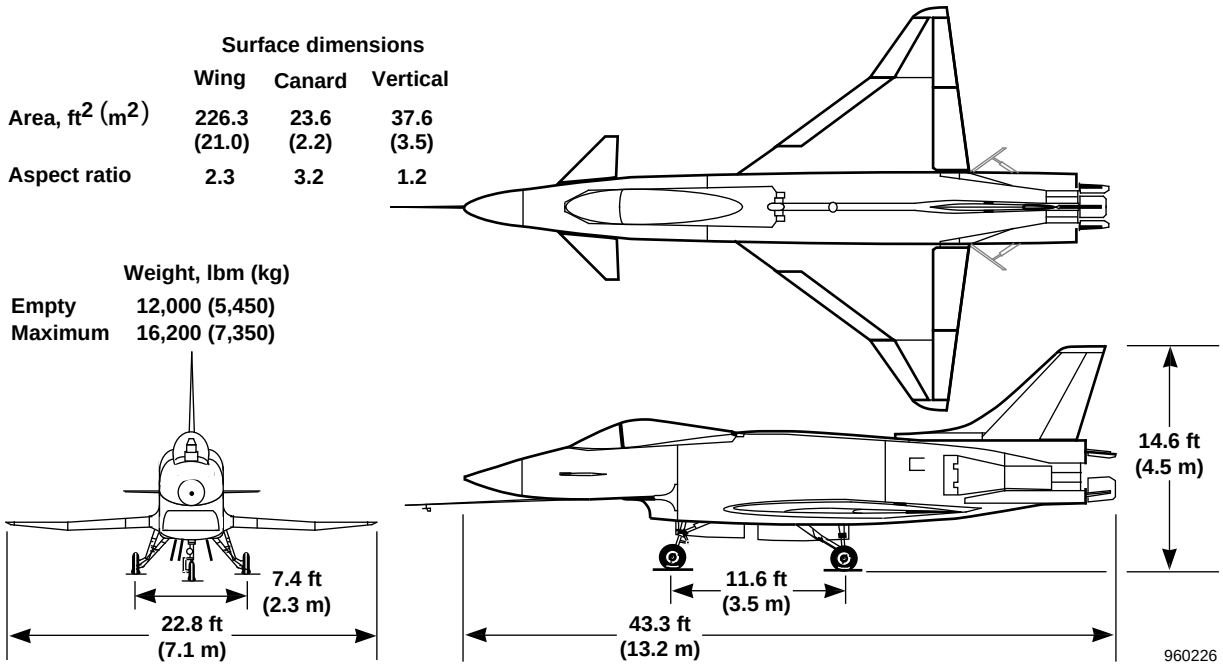

Figure 2. Three-view drawing of X-31A aircraft.

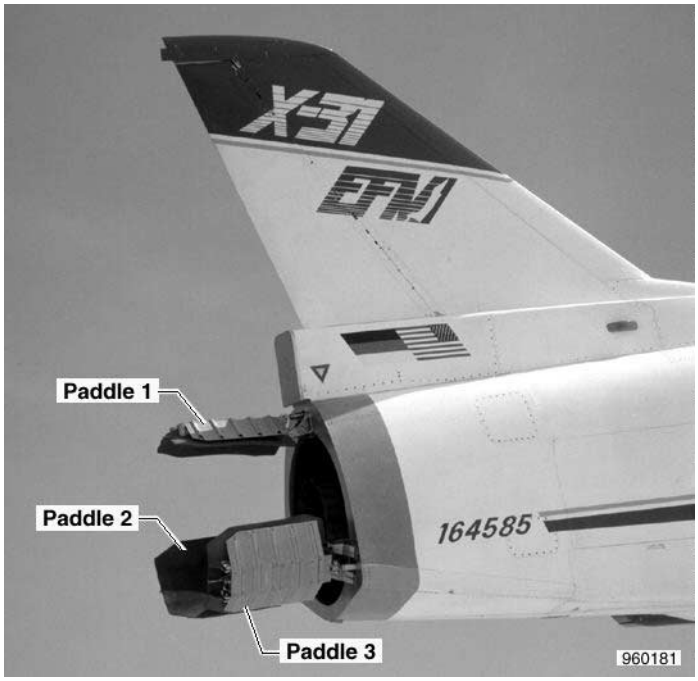

Figure 3. Arrangement of thrust-vector vanes.

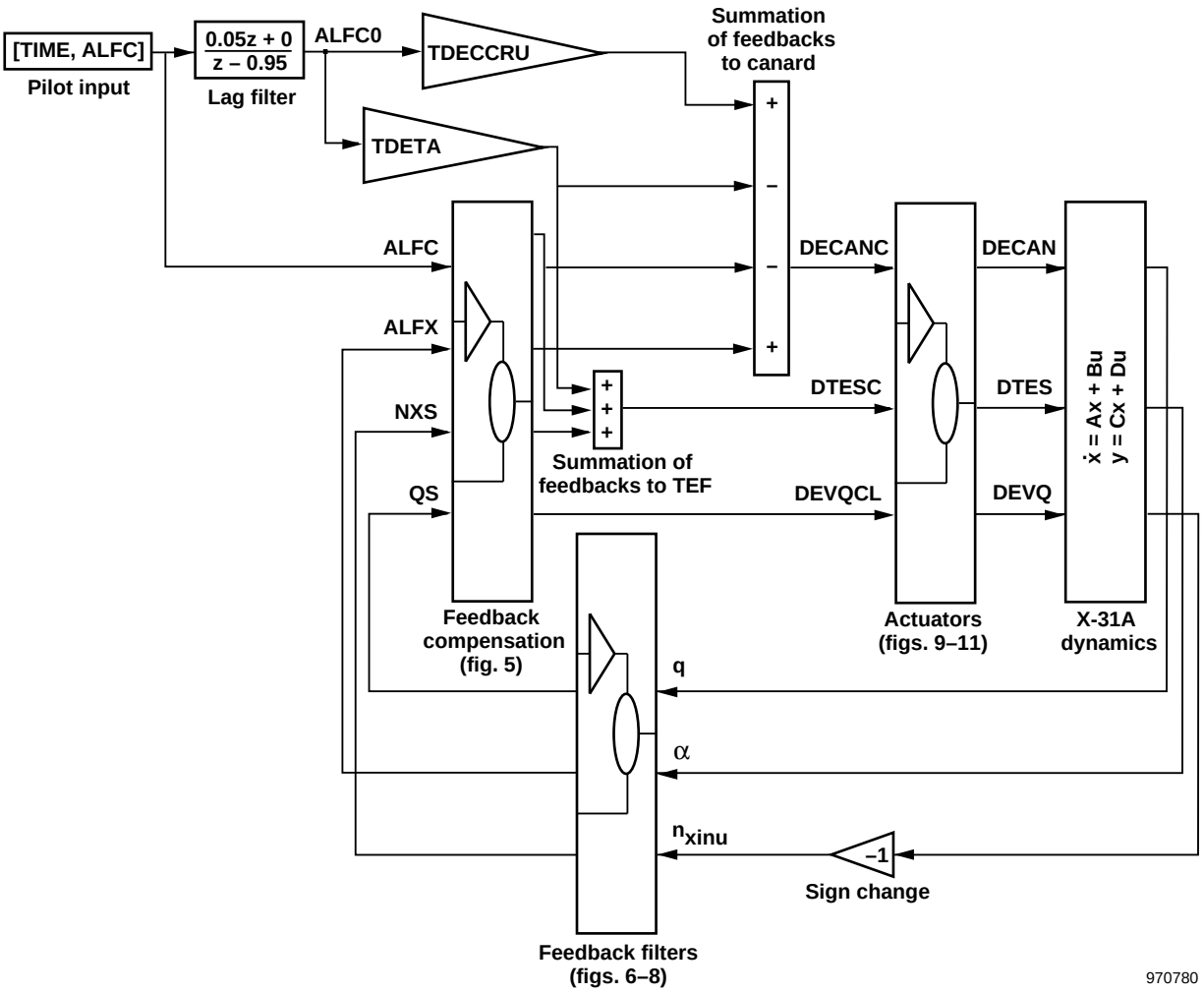

Figure 4. Longitudinal control system linear model.

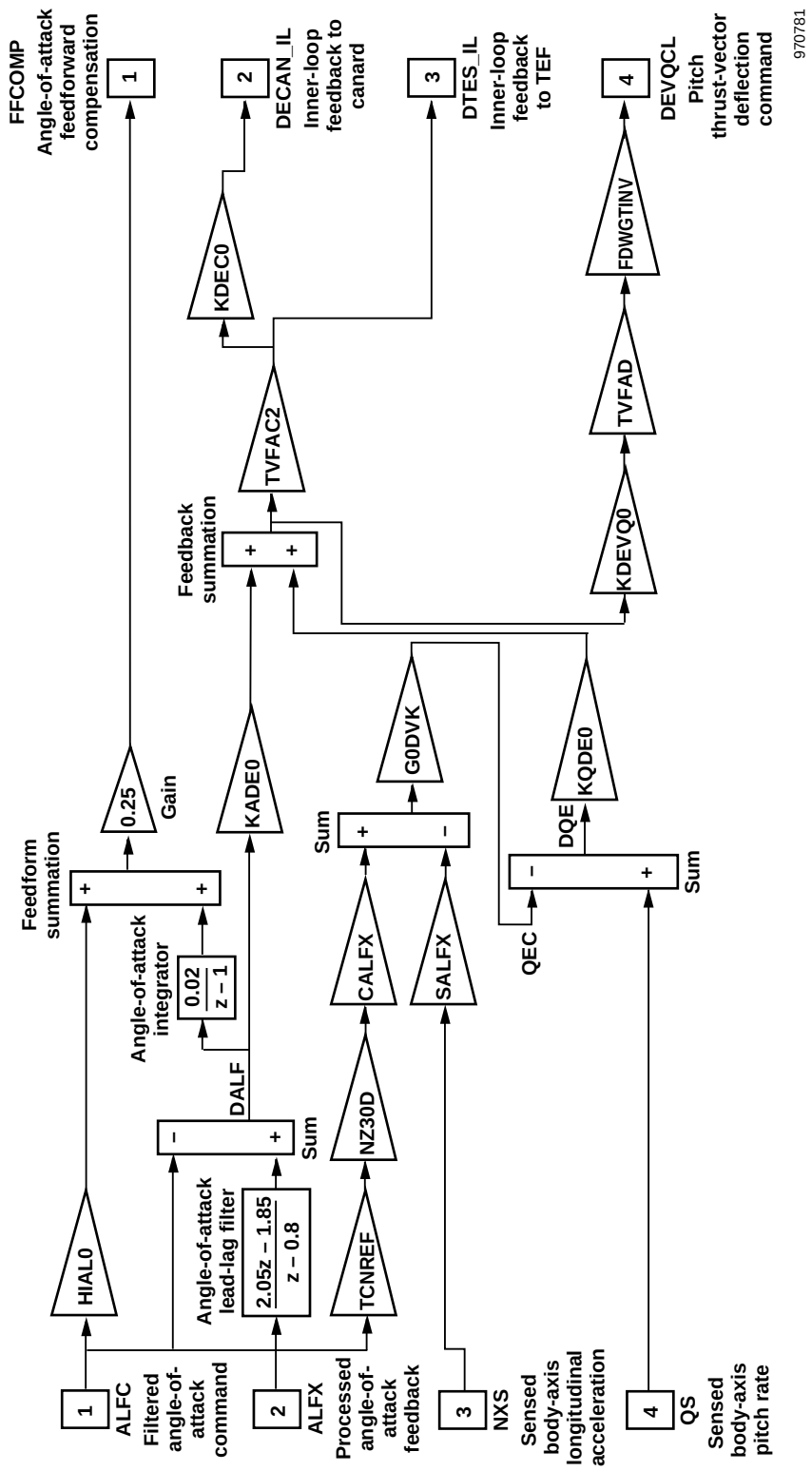

Figure 5. Feedback compensation for the longitudinal axis.

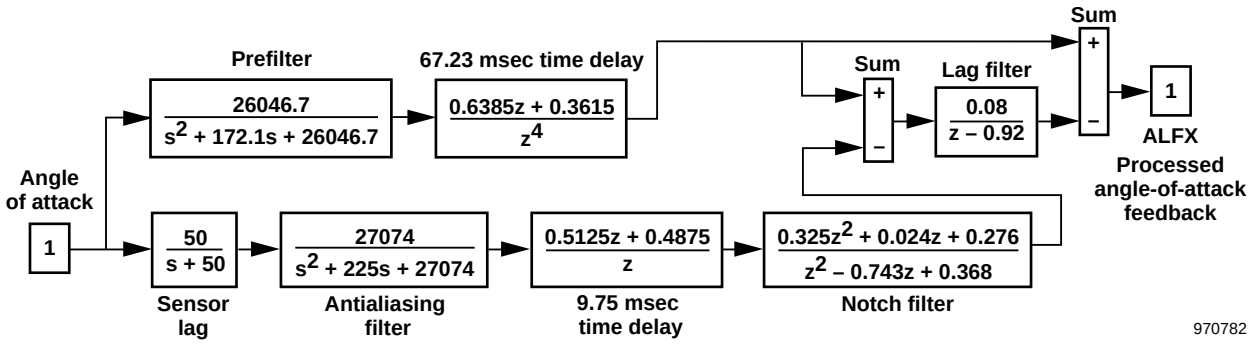

Figure 6. Processing for angle-of-attack feedback.

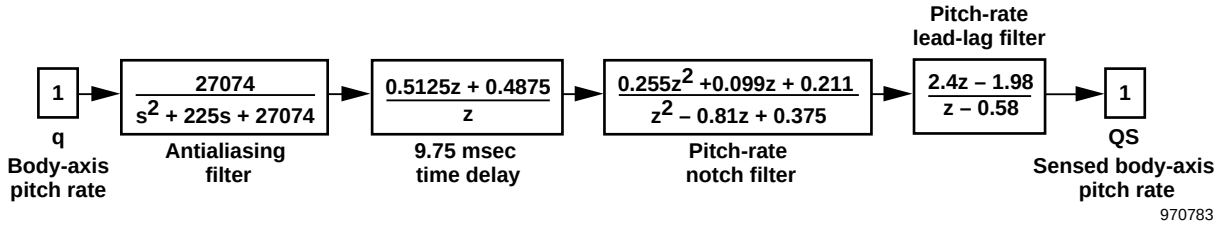

Figure 7. Filtering for pitch-rate feedback.

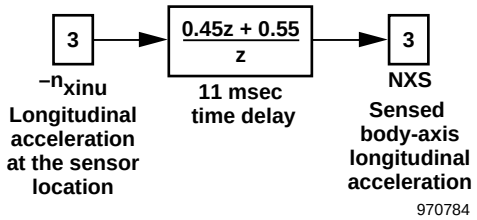

Figure 8. Filtering for axial-acceleration feedback.

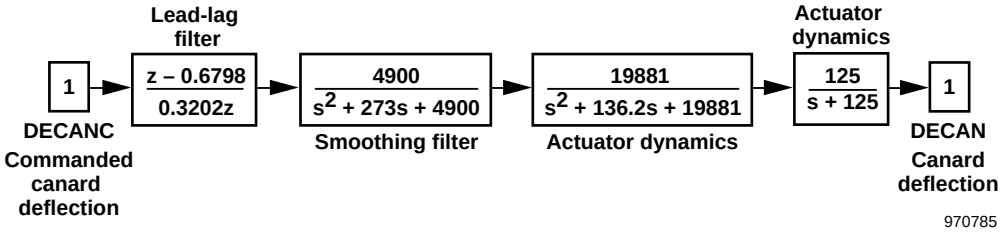

Figure 9. Filters and actuator models for the canard.

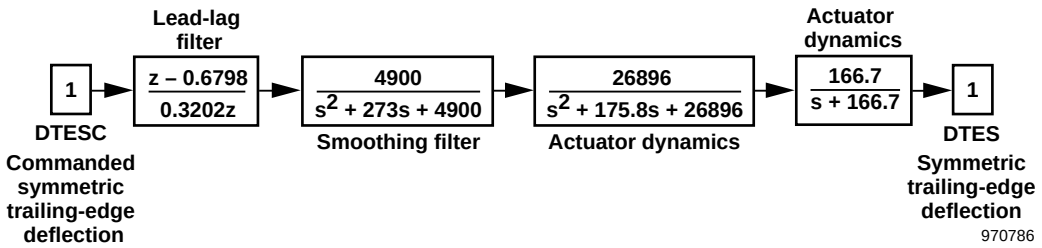

Figure 10. Filter and actuator models for the trailing-edge flaps.

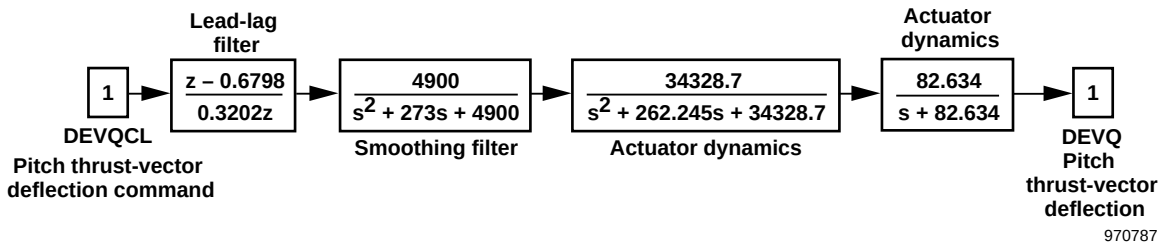

Figure 11. Filter and actuator models for pitch thrust vectoring.

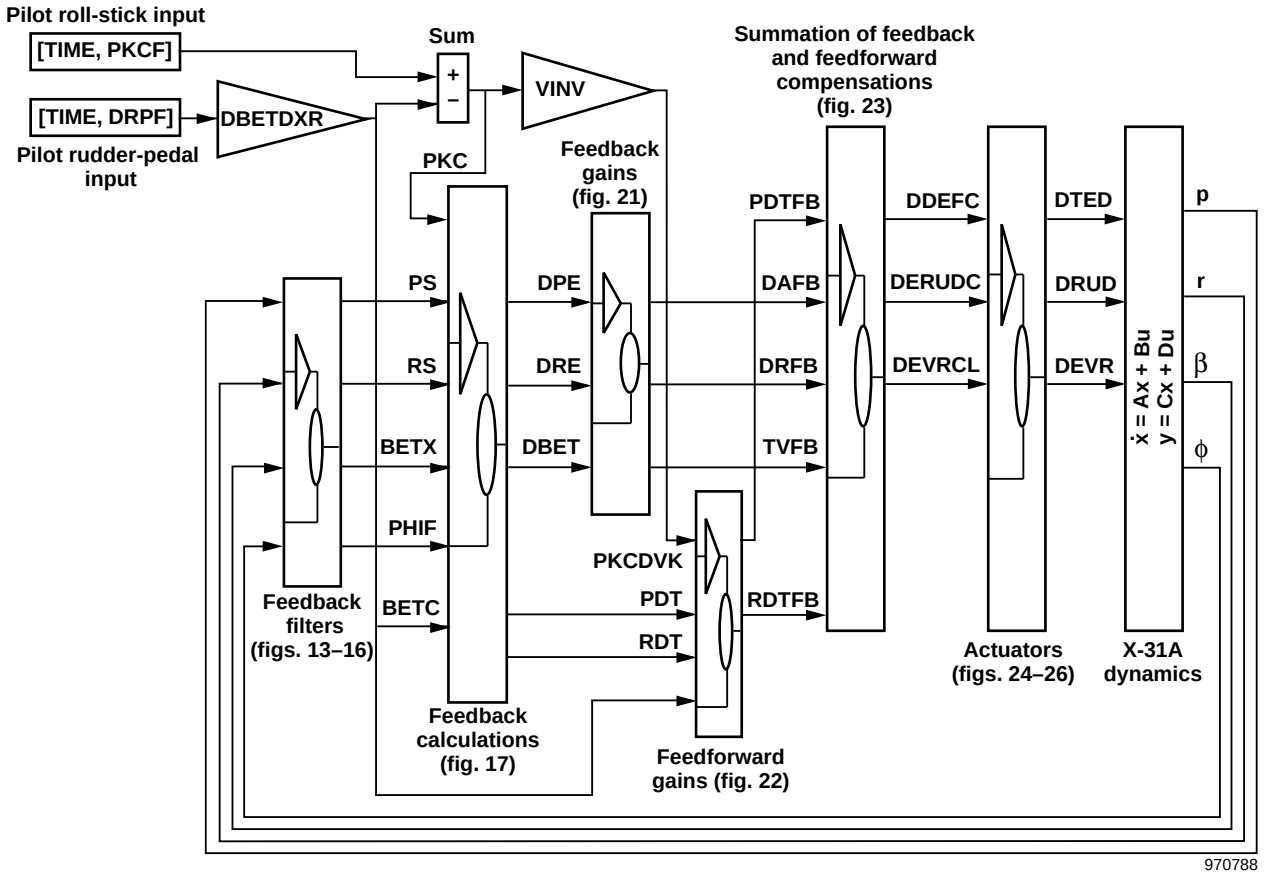

Figure 12. Lateral-directional control system linear model.

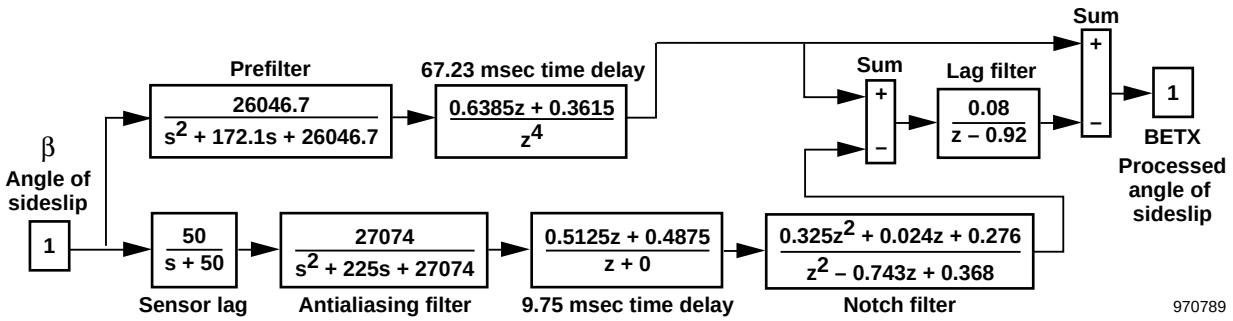

Figure 13. Processing for angle-of-sideslip feedback.

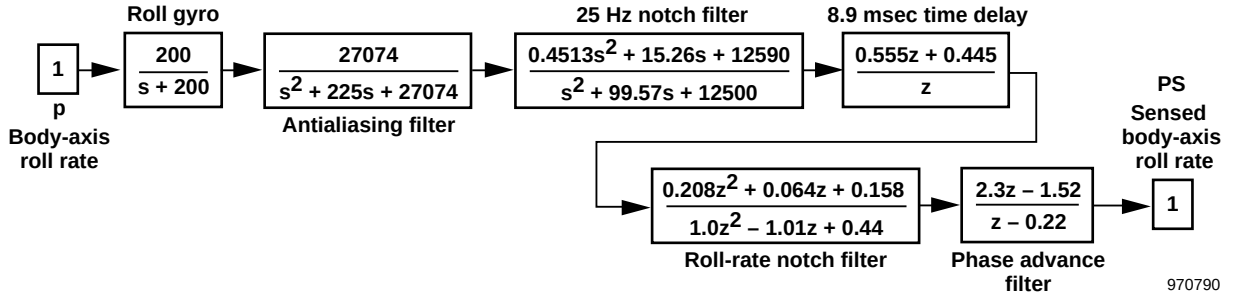

Figure 14. Filters for roll-rate feedback.

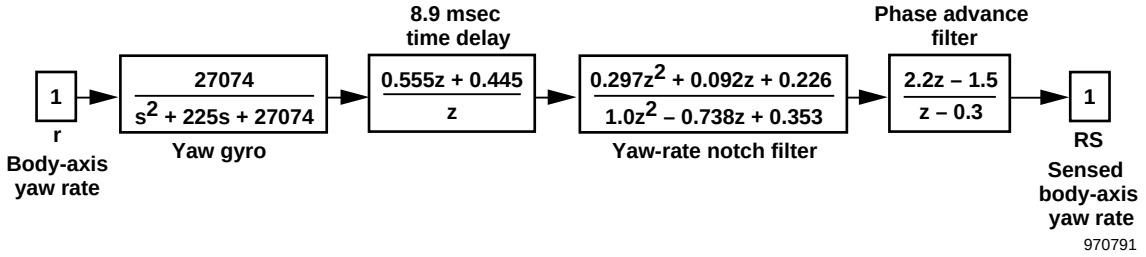

Figure 15. Filters for yaw-rate feedback.

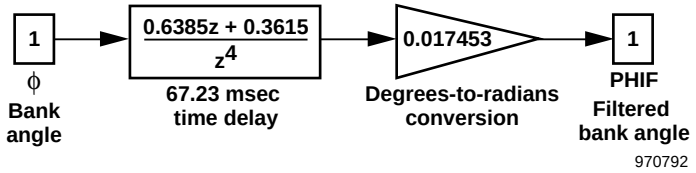

Figure 16. Filters for bank-angle feedback.

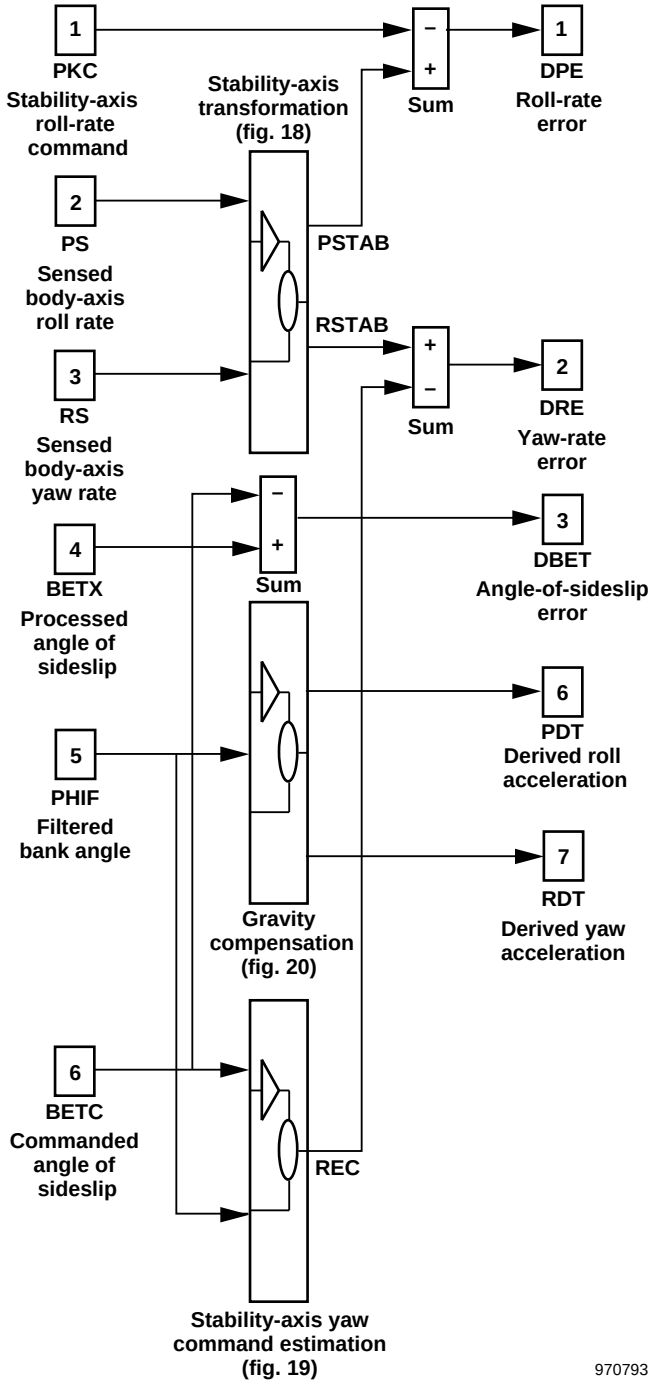

Figure 17. Feedback calculations.

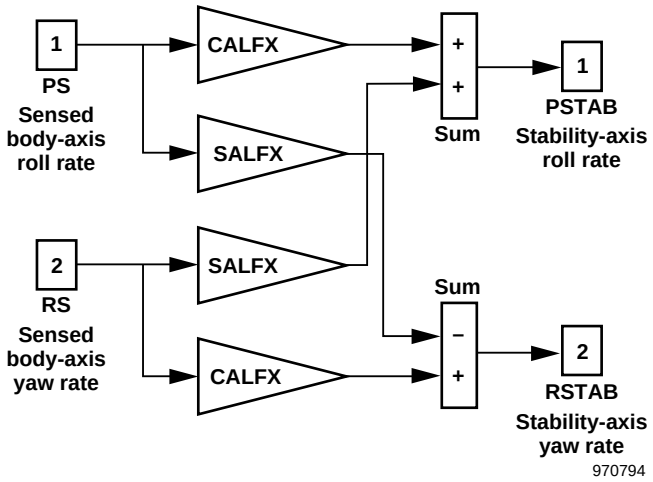

Figure 18. Stability-axis transformation for lateral-directional feedbacks.

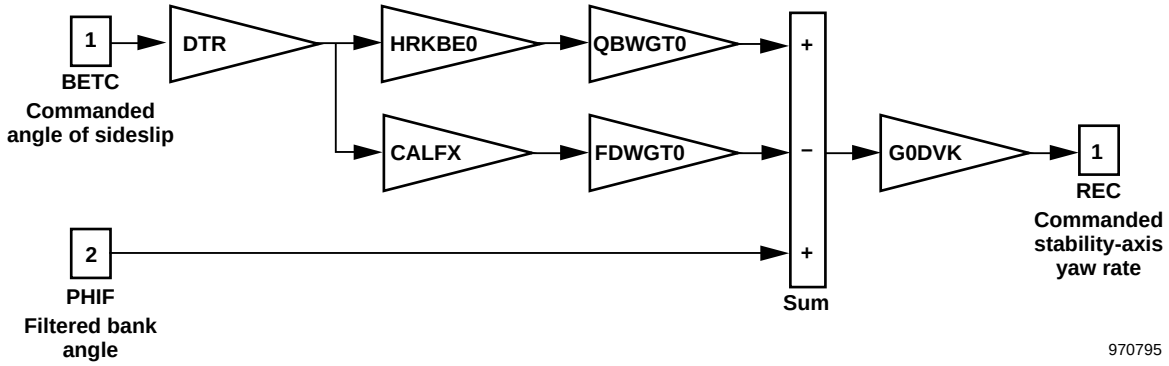

Figure 19. Calculation of stability-axis yaw-rate command.

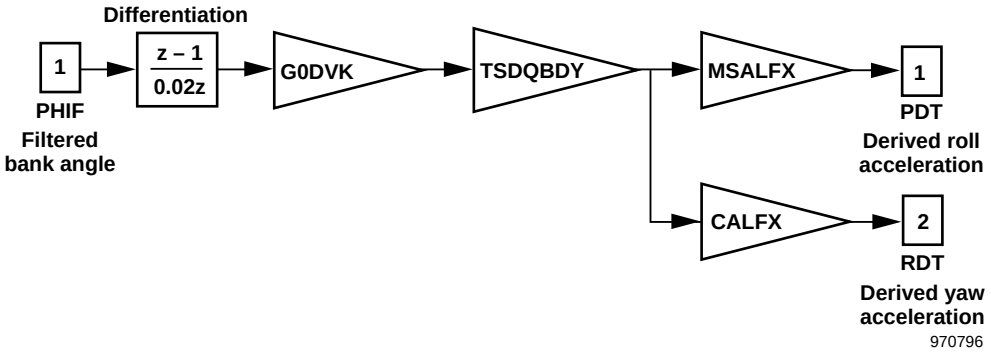

Figure 20. Linear model of gravity compensation.

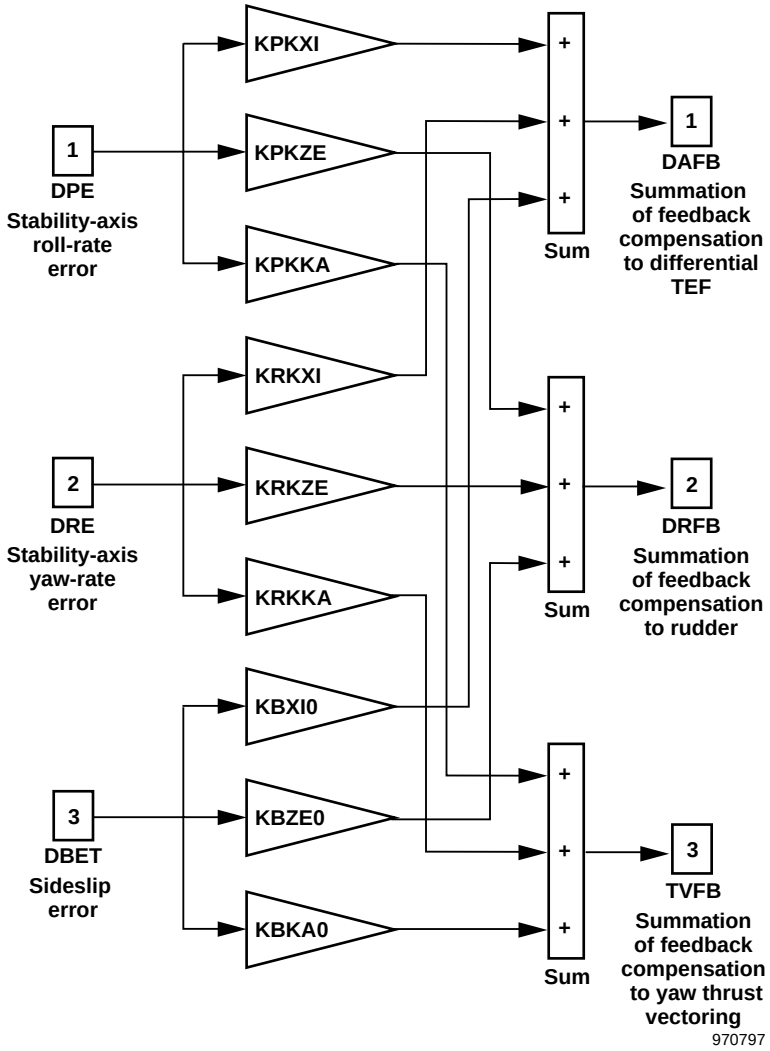

Figure 21. Lateral-directional axes feedback gain compensation.

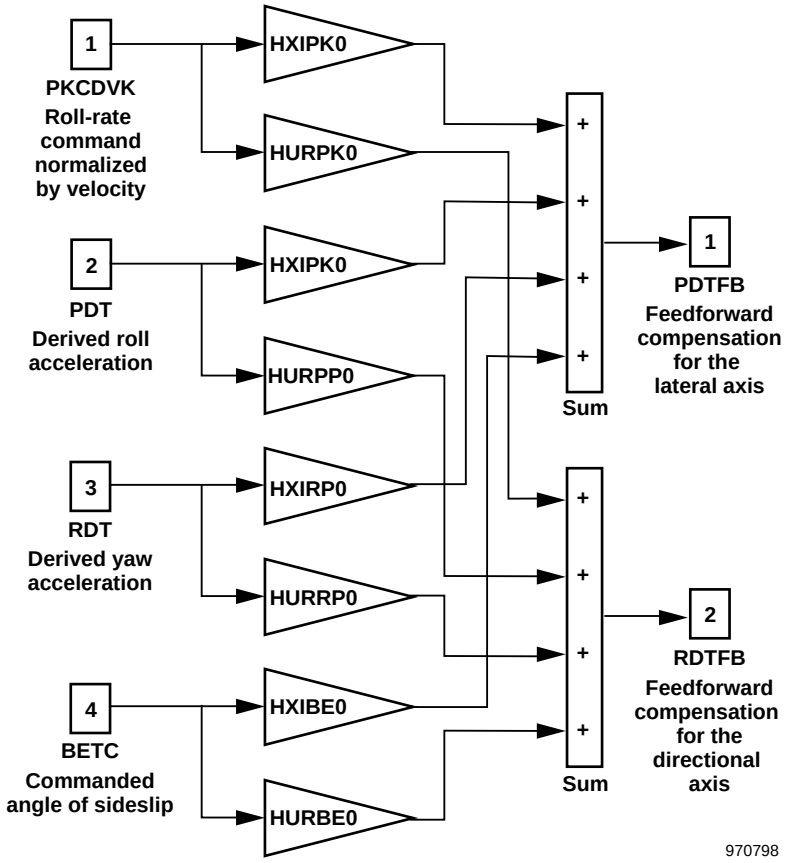

Figure 22. Lateral-directional axes forward-path compensation.

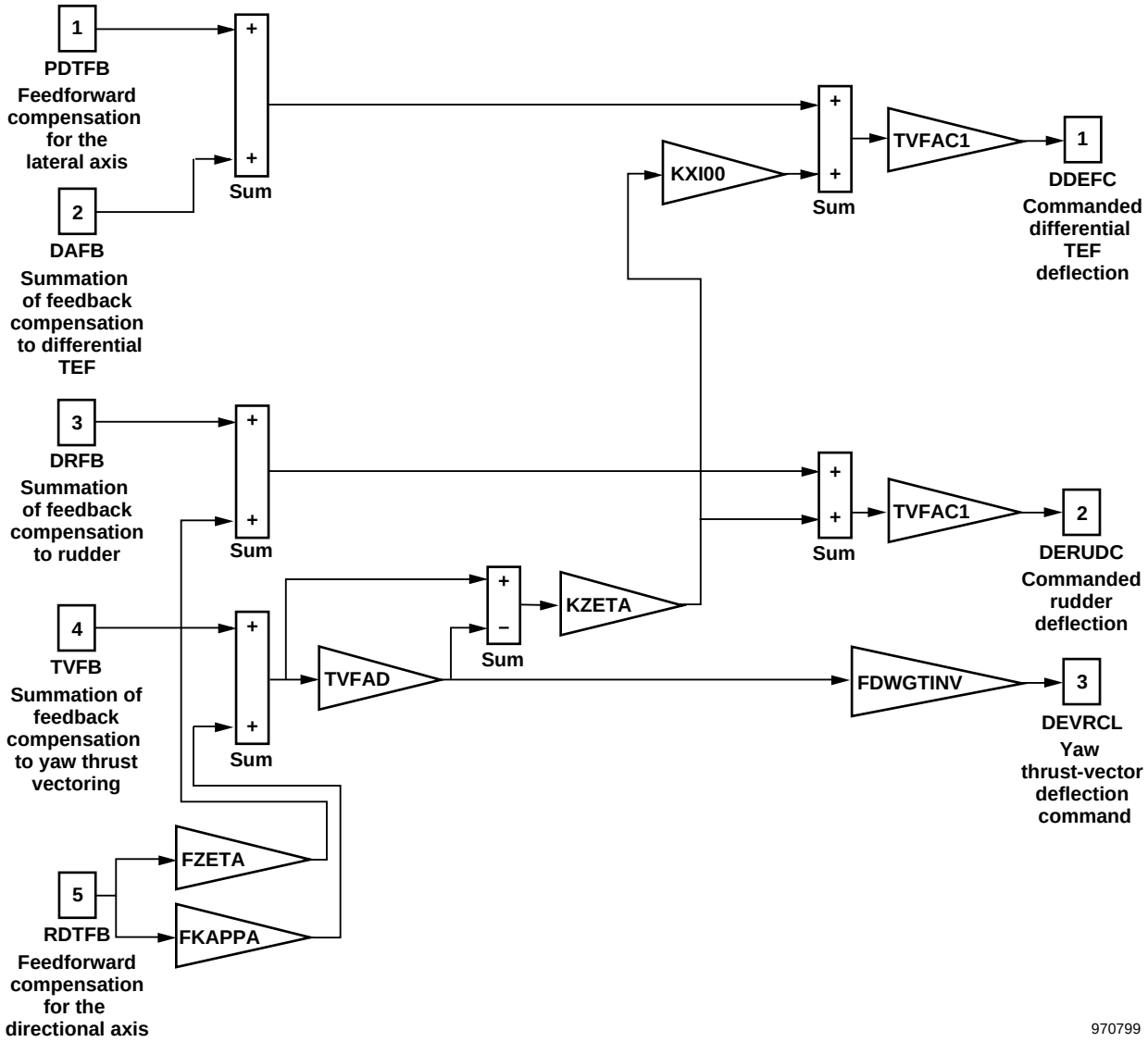

Figure 23. Summation of feedback and feedforward compensations.

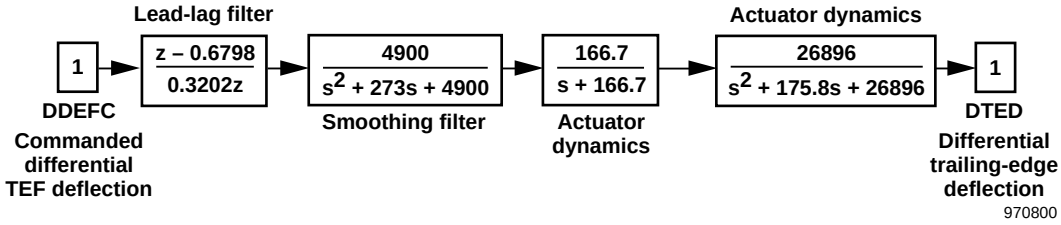

Figure 24. Filters and actuator models for the differential trailing-edge flaps.

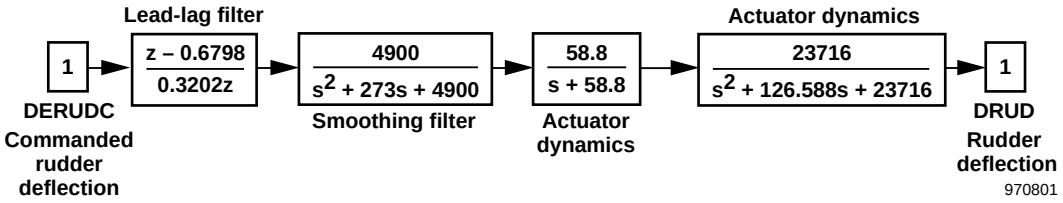

Figure 25. Filters and actuator models for the rudder.

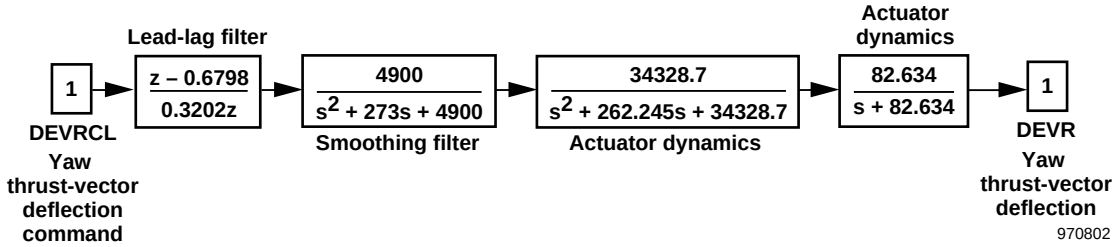

Figure 26. Filters and actuator models for yaw thrust vectoring.

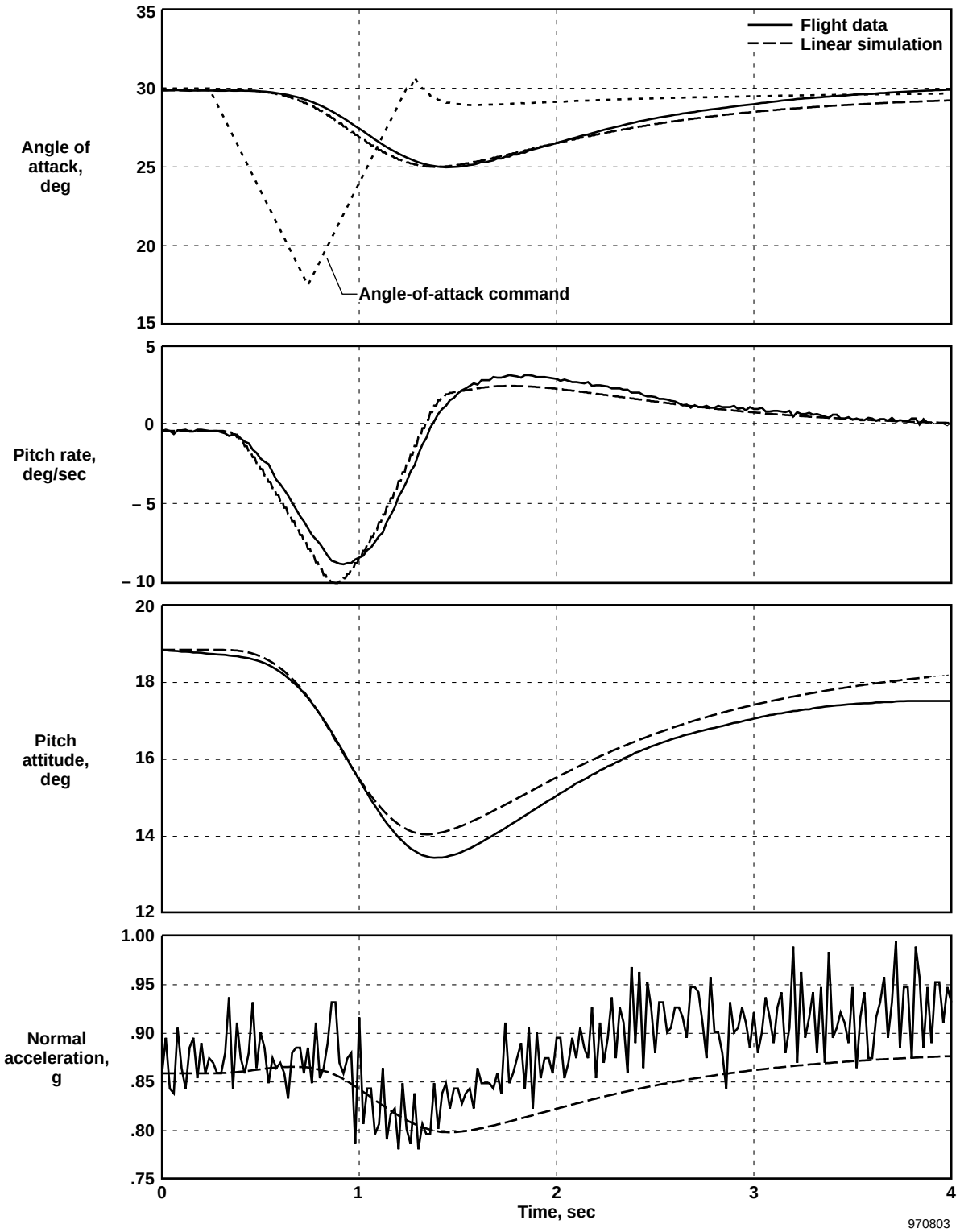

(a) Comparison of linear simulation response with flight data for a pitch doublet at 30° angle of attack.

Figure 27. Comparison between flight and simulation data at 30° angle of attack.

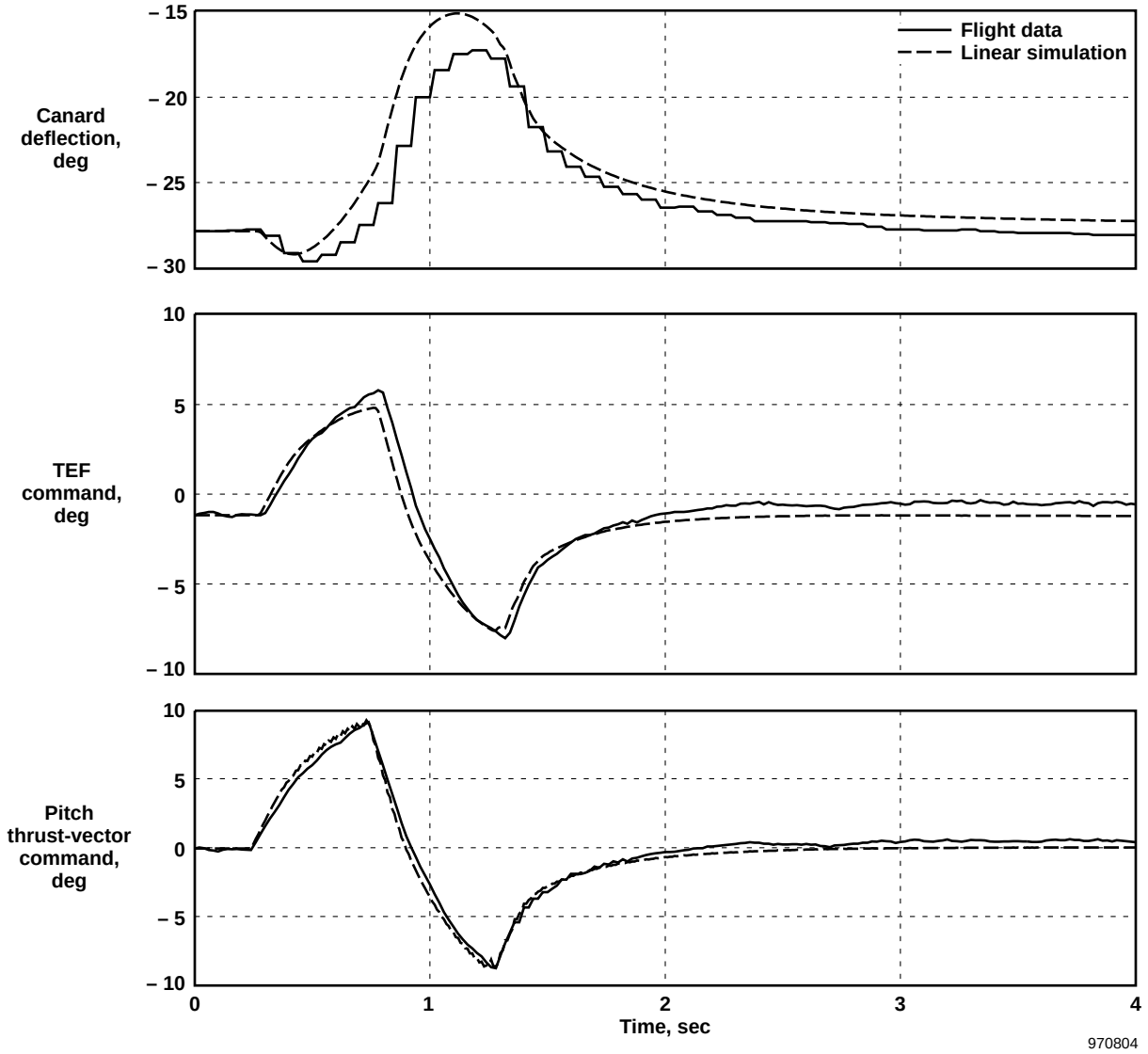

(b) Comparison of linear simulation response with flight data for a pitch doublet at 30° angle of attack.

Figure 27. Concluded.

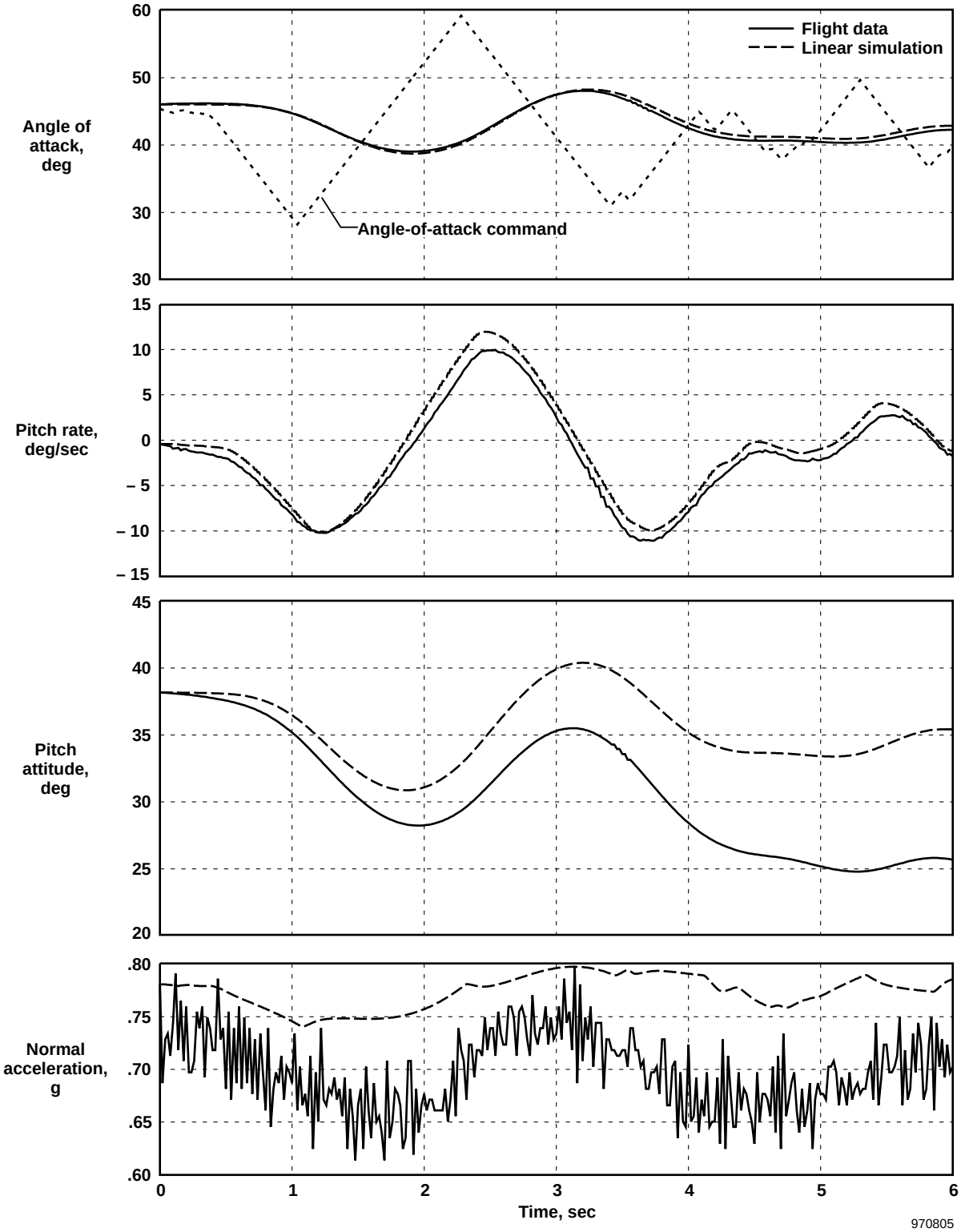

(a) Comparison of linear simulation response with flight data for a pitch doublet at 45° angle of attack.

Figure 28. Comparison between flight and simulation data at 45° angle of attack.

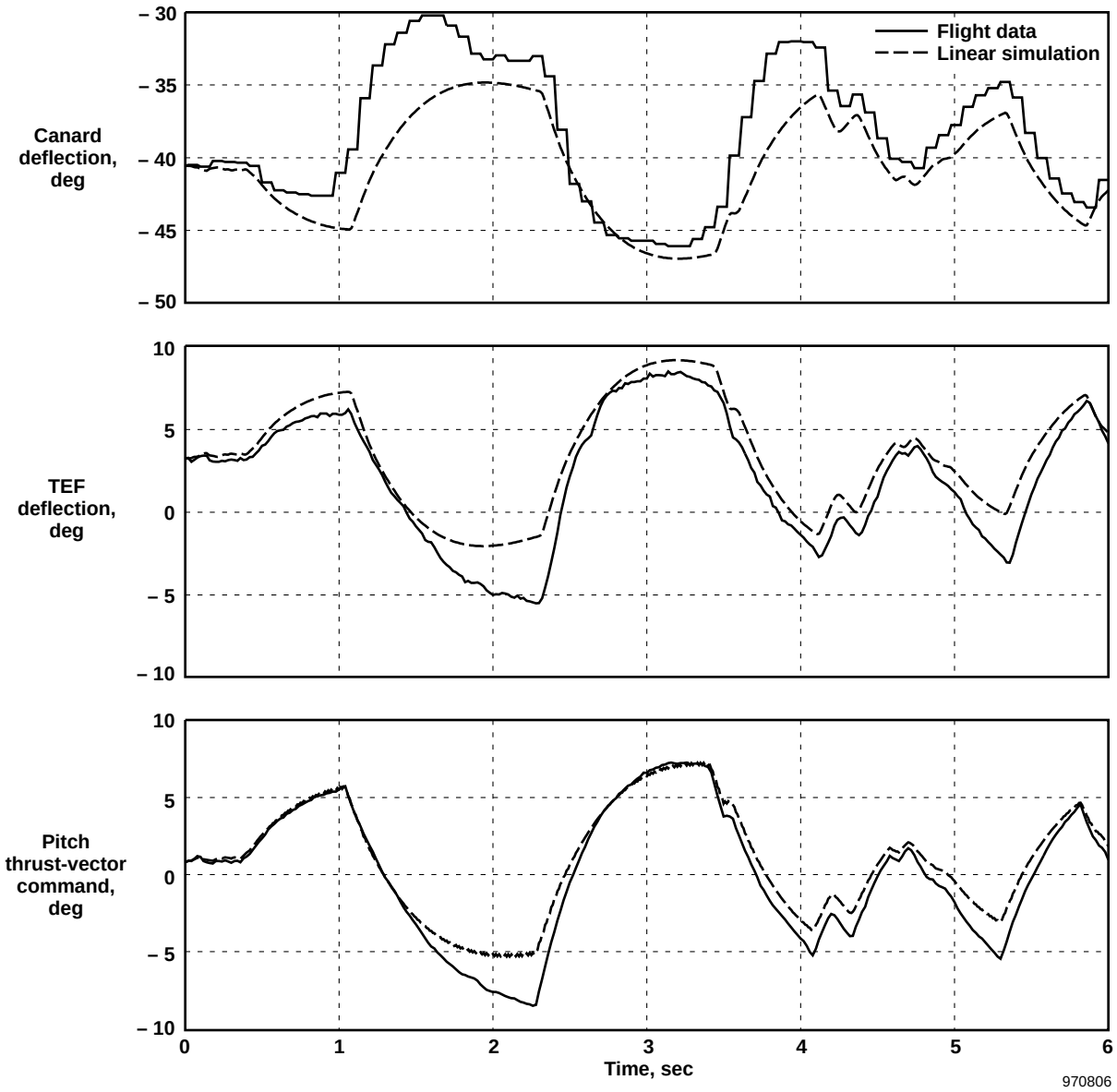

(b) Comparison of linear simulation response with flight data for a pitch doublet at 45° angle of attack.

Figure 28. Concluded.

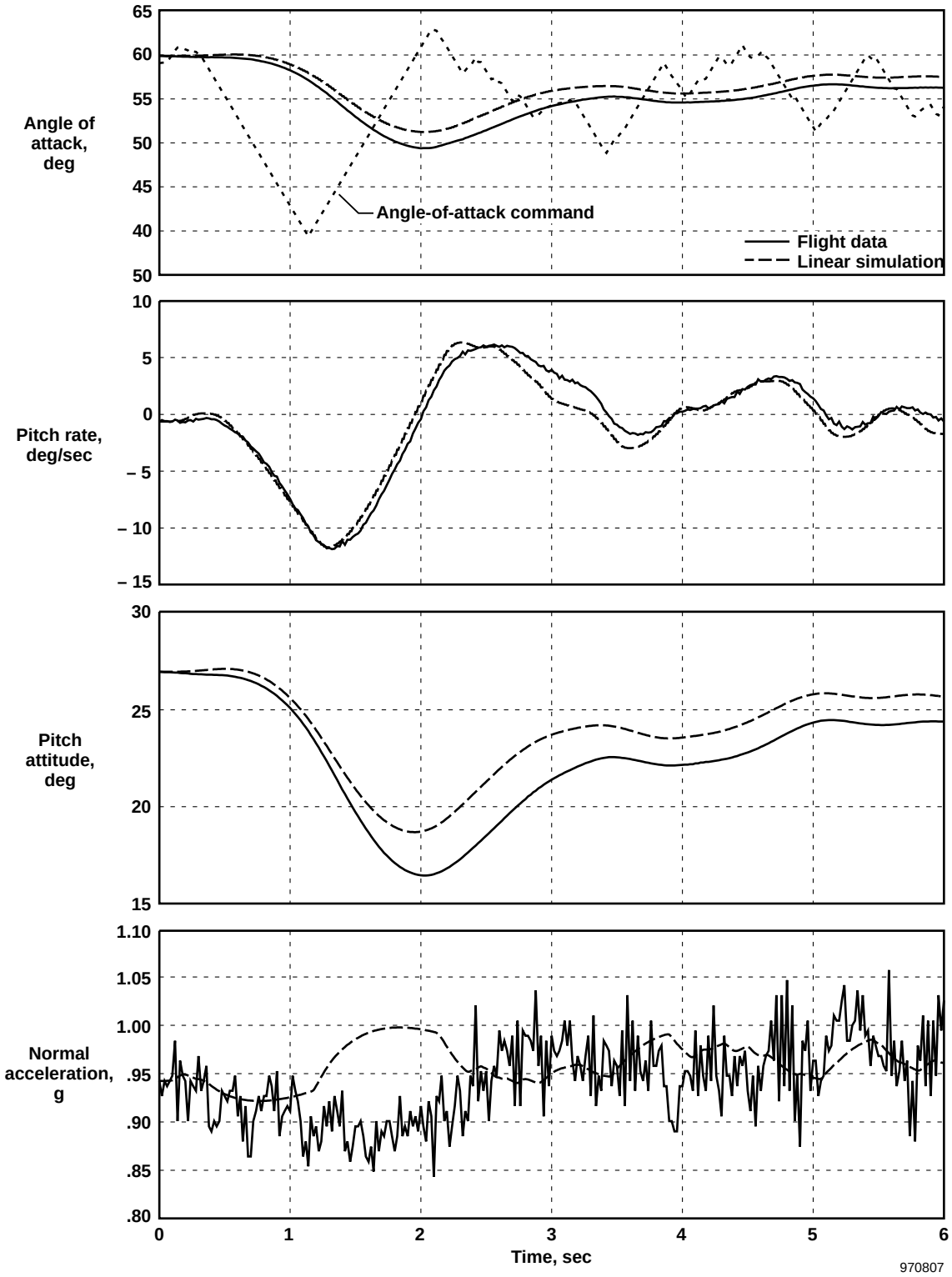

(a) Comparison of linear simulation response with flight data for a pitch doublet at 60° angle of attack.

Figure 29. Comparison between flight and simulation data at 60° angle of attack.

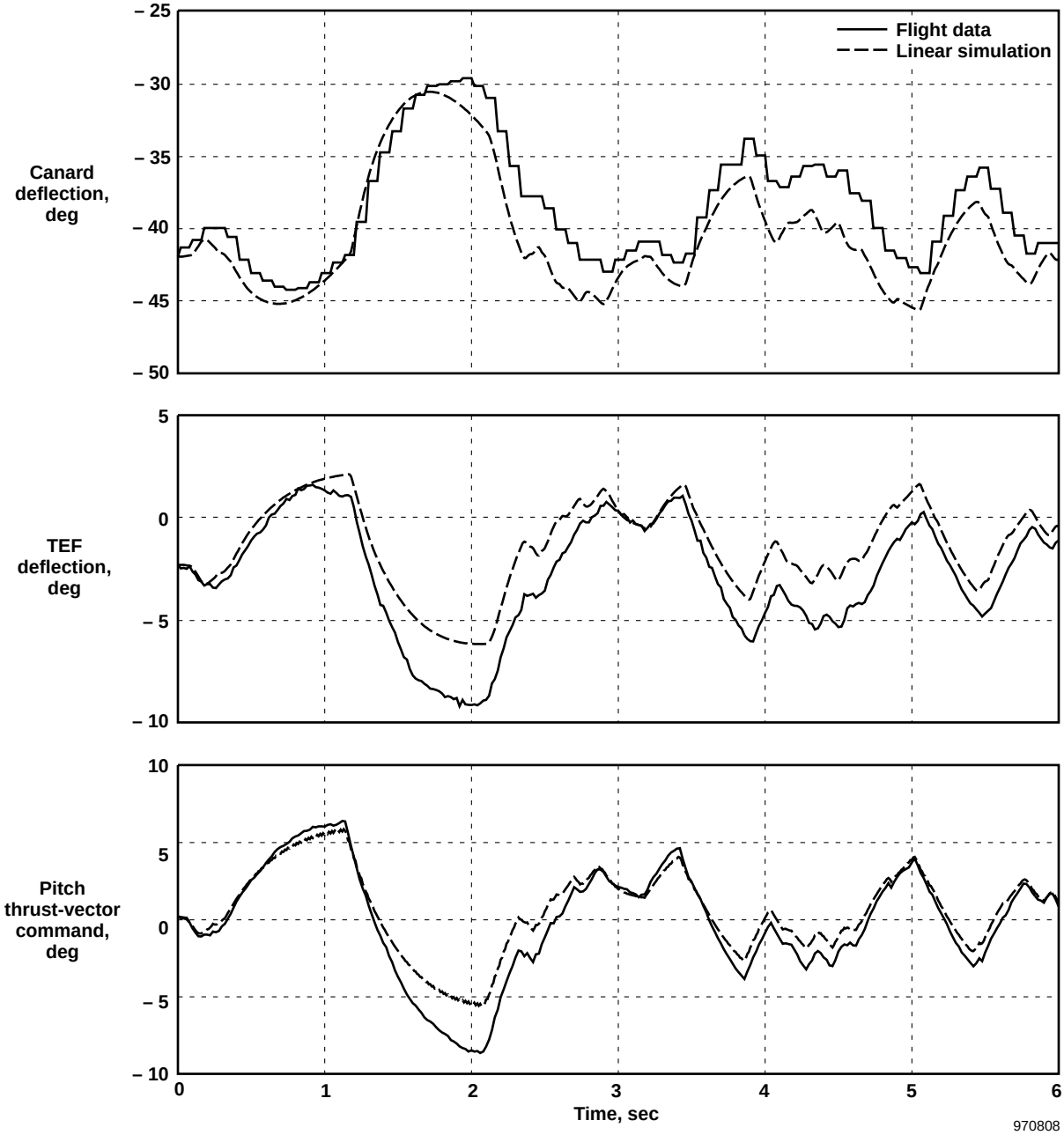

(b) Comparison of linear simulation response with flight data for a pitch doublet at 60° angle of attack.

Figure 29. Concluded.

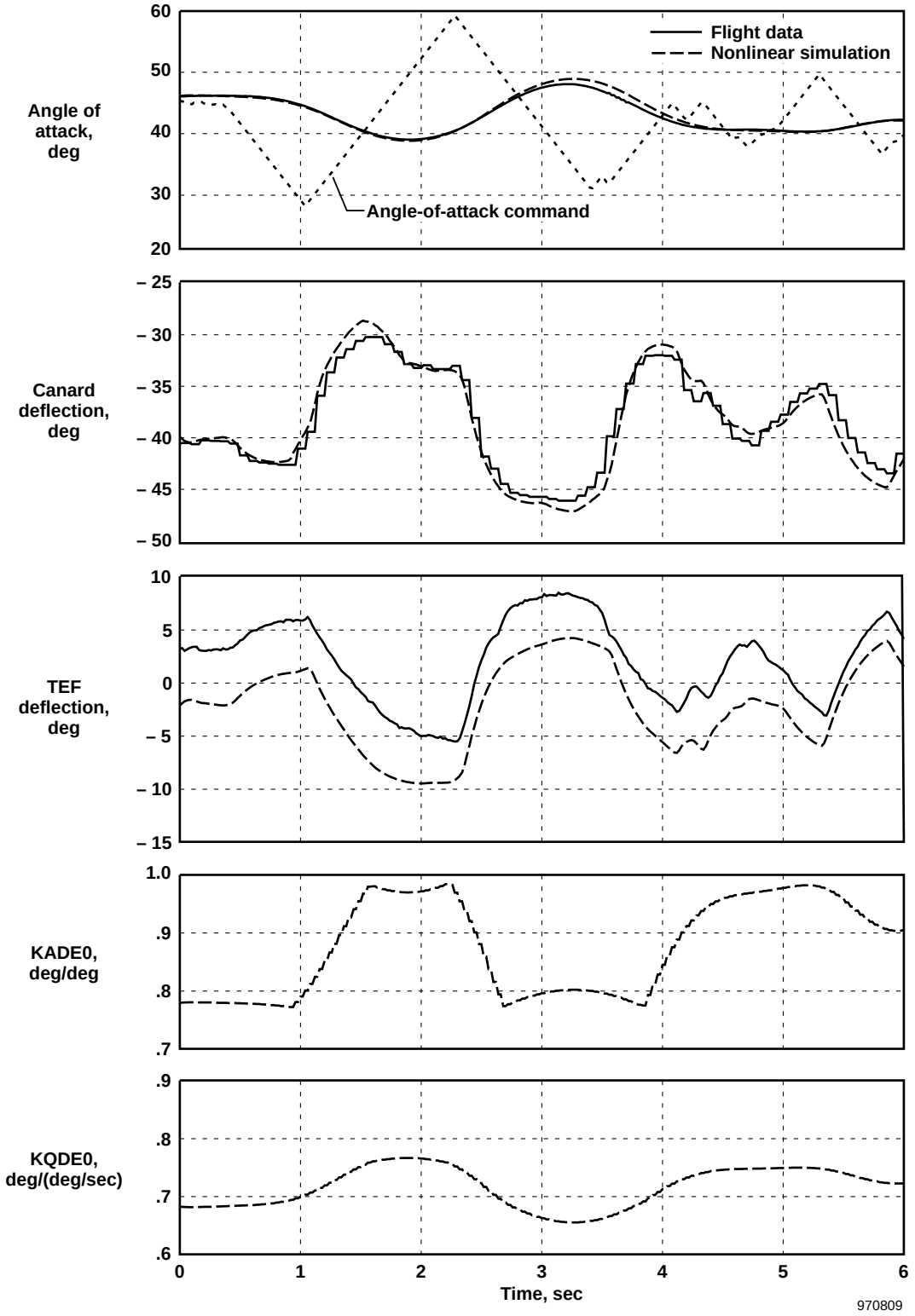

Figure 30. Comparison of nonlinear simulation response with flight data for a pitch doublet at 45° angle of attack.

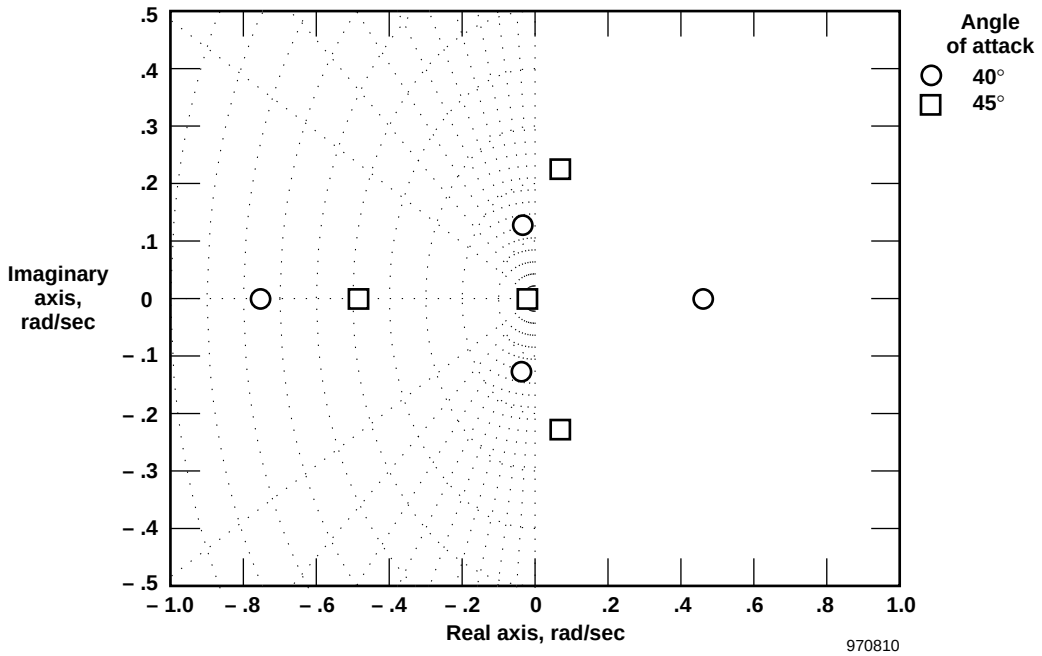

Figure 31. Comparison of bare airframe longitudinal axis roots at 40° and 45° angle of attack.

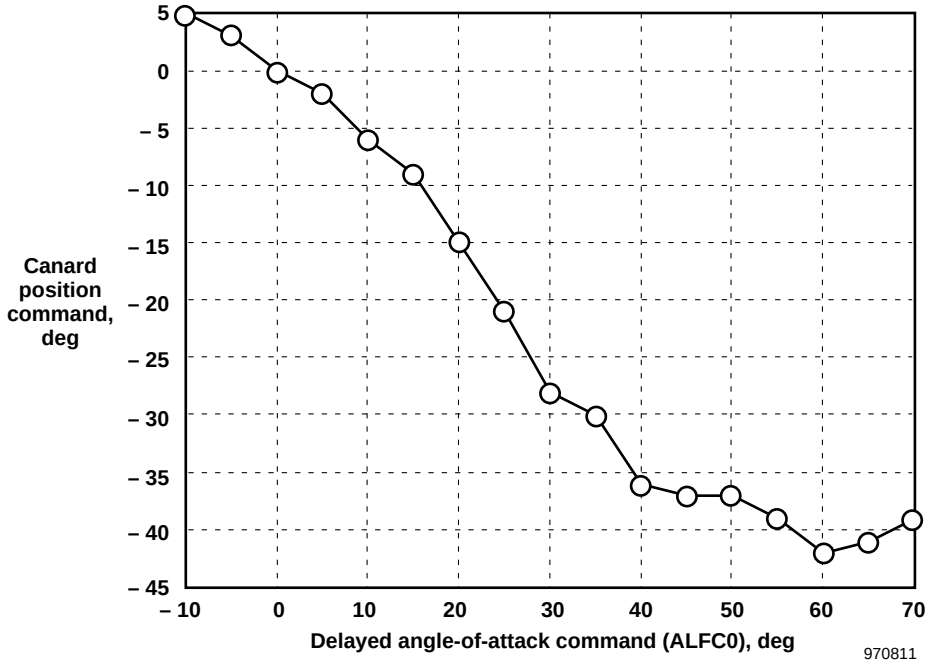

Figure 32. Feedforward gain from angle of attack to canard.

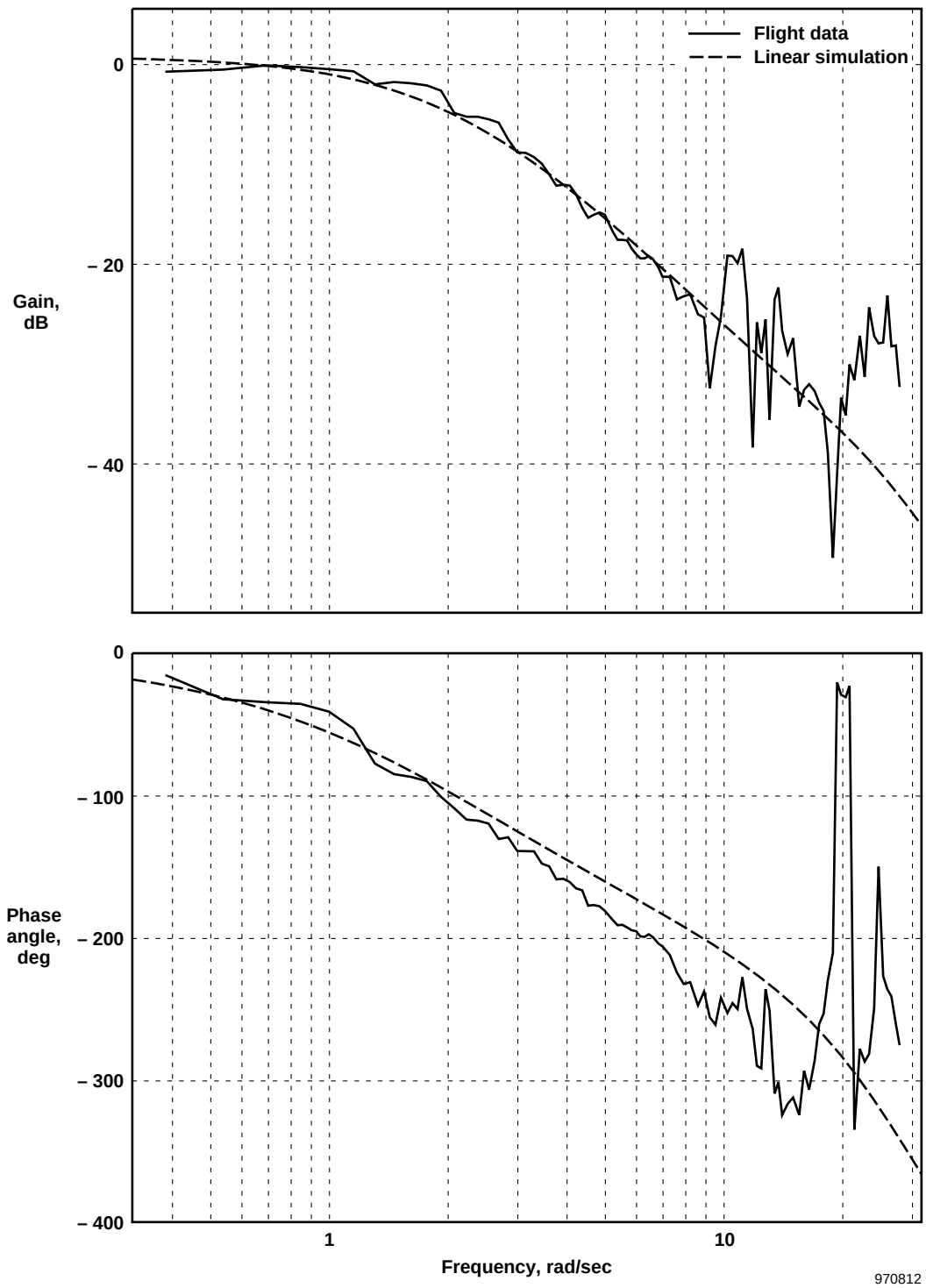

Figure 33. Frequency response comparison between linear simulation and flight data for *ALFX*/*ALFC* at 30° angle of attack.

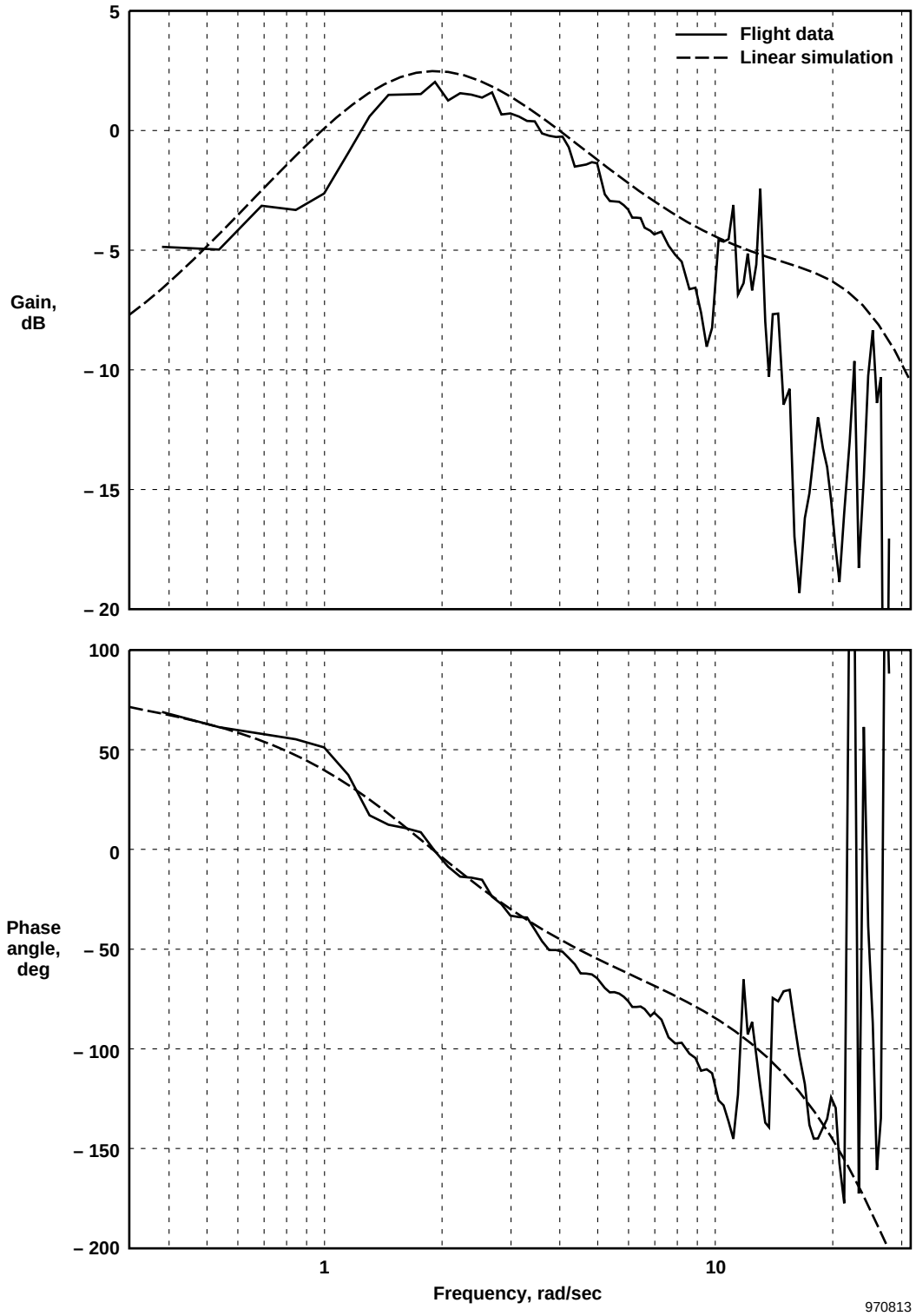

Figure 34. Frequency response comparison between linear simulation and flight data for *Q*/*ALFC* at 30° angle of attack.

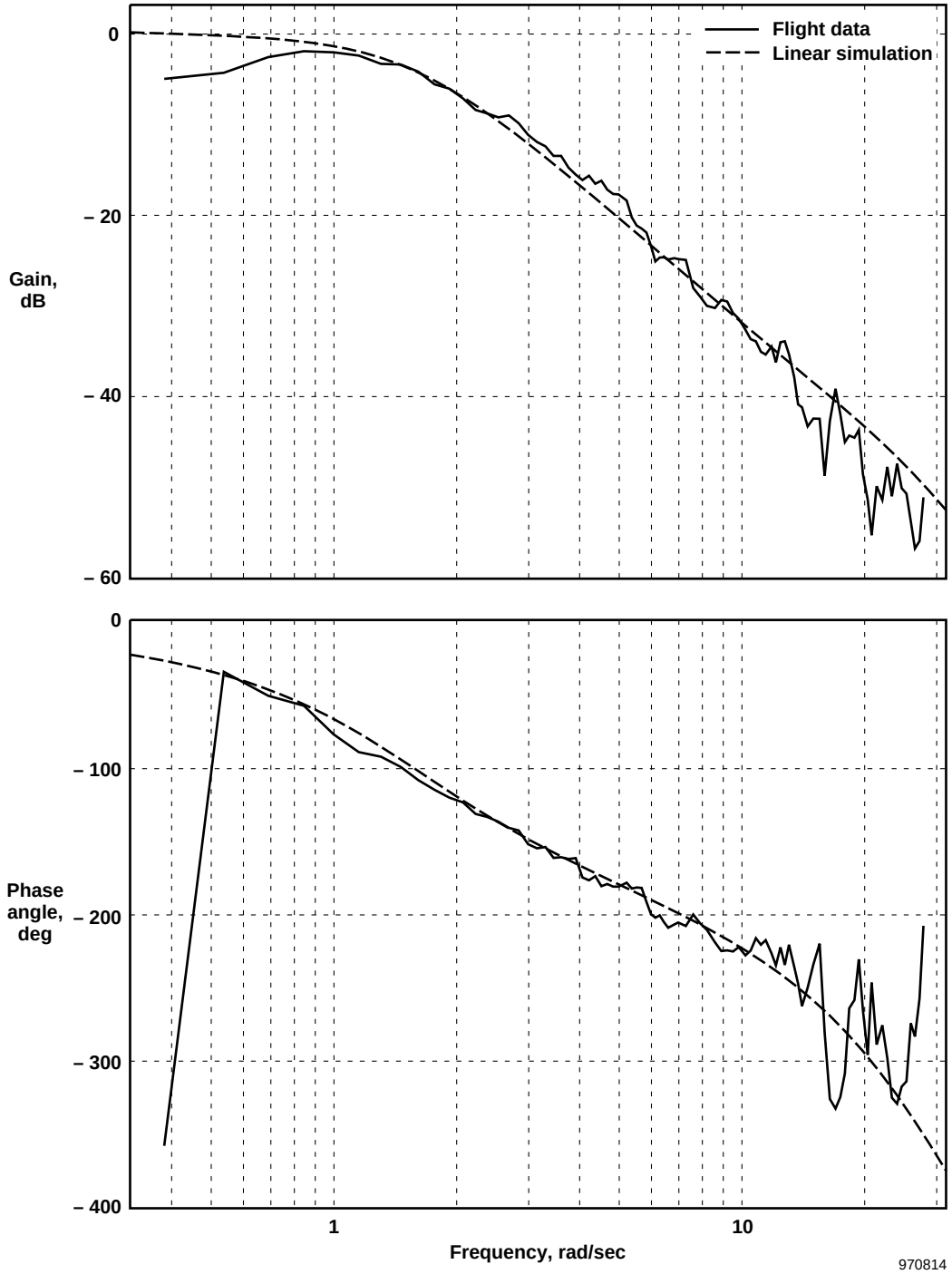

Figure 35. Frequency response comparison between linear simulation and flight data for *ALFX*/*ALFC* at 45° angle of attack.

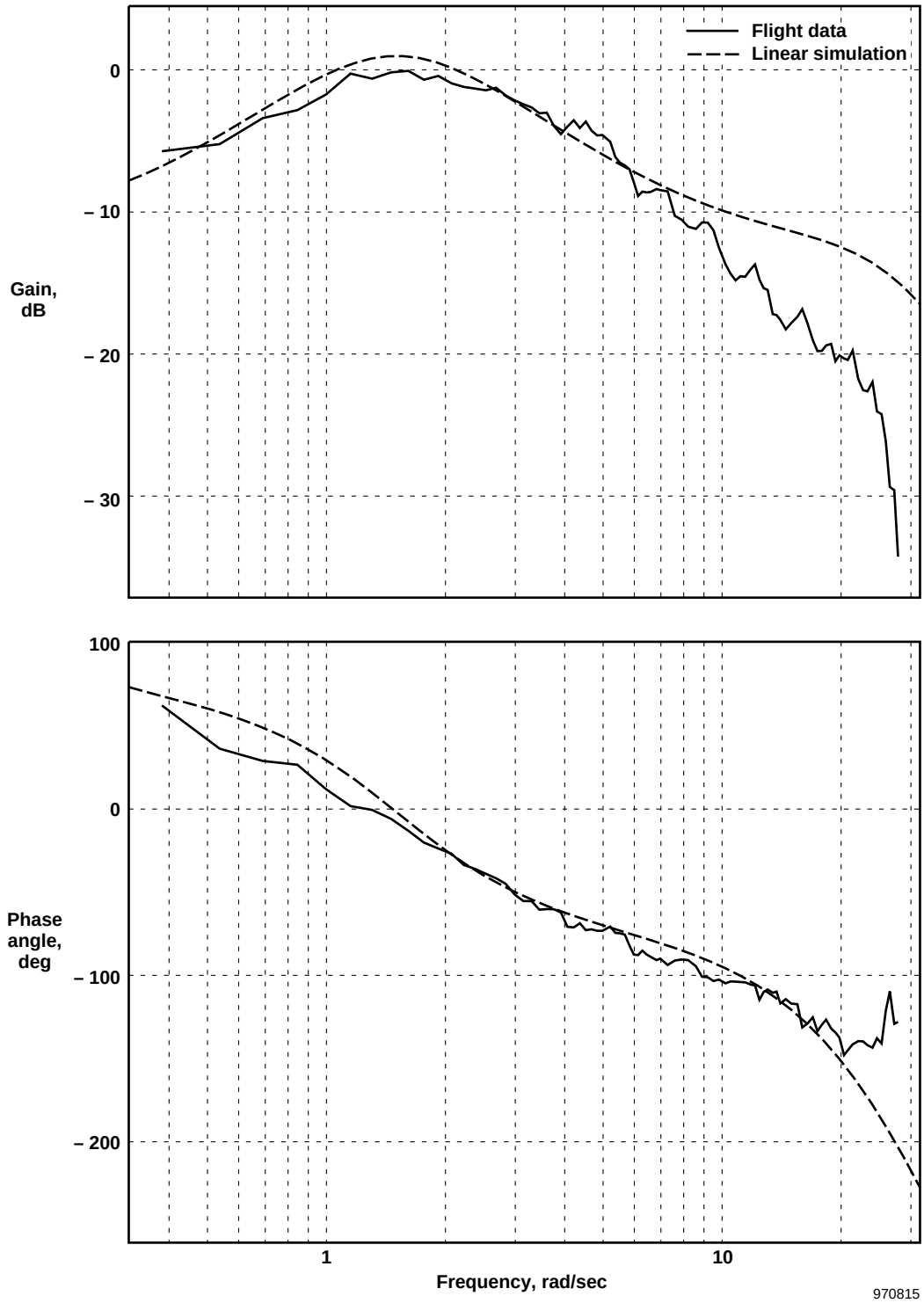

Figure 36. Frequency response comparison between linear simulation and flight data for *Q*/*ALFC* at 45° angle of attack.

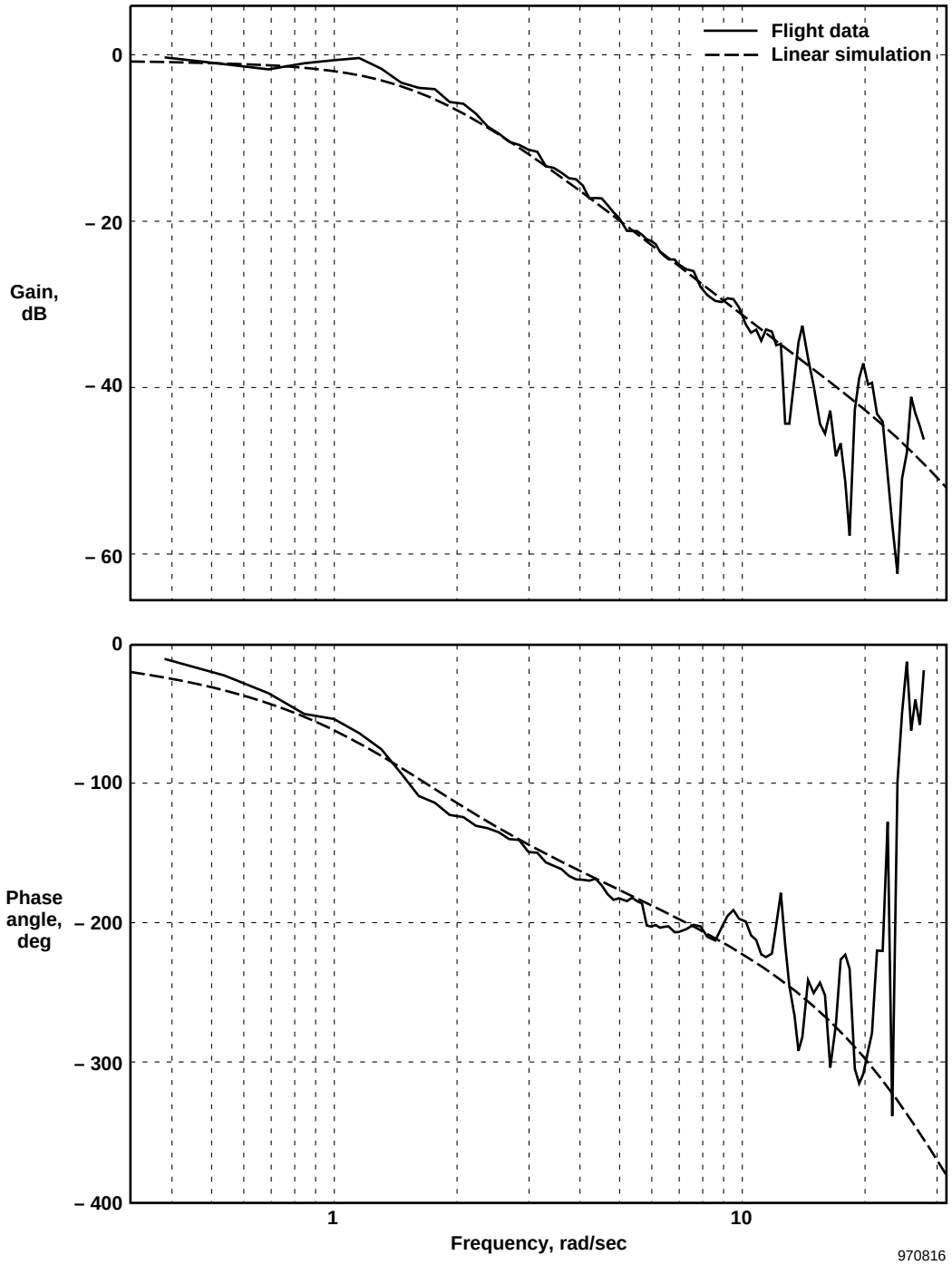

Figure 37. Frequency response comparison between linear simulation and flight data for *ALFX*/*ALFC* at 60° angle of attack.

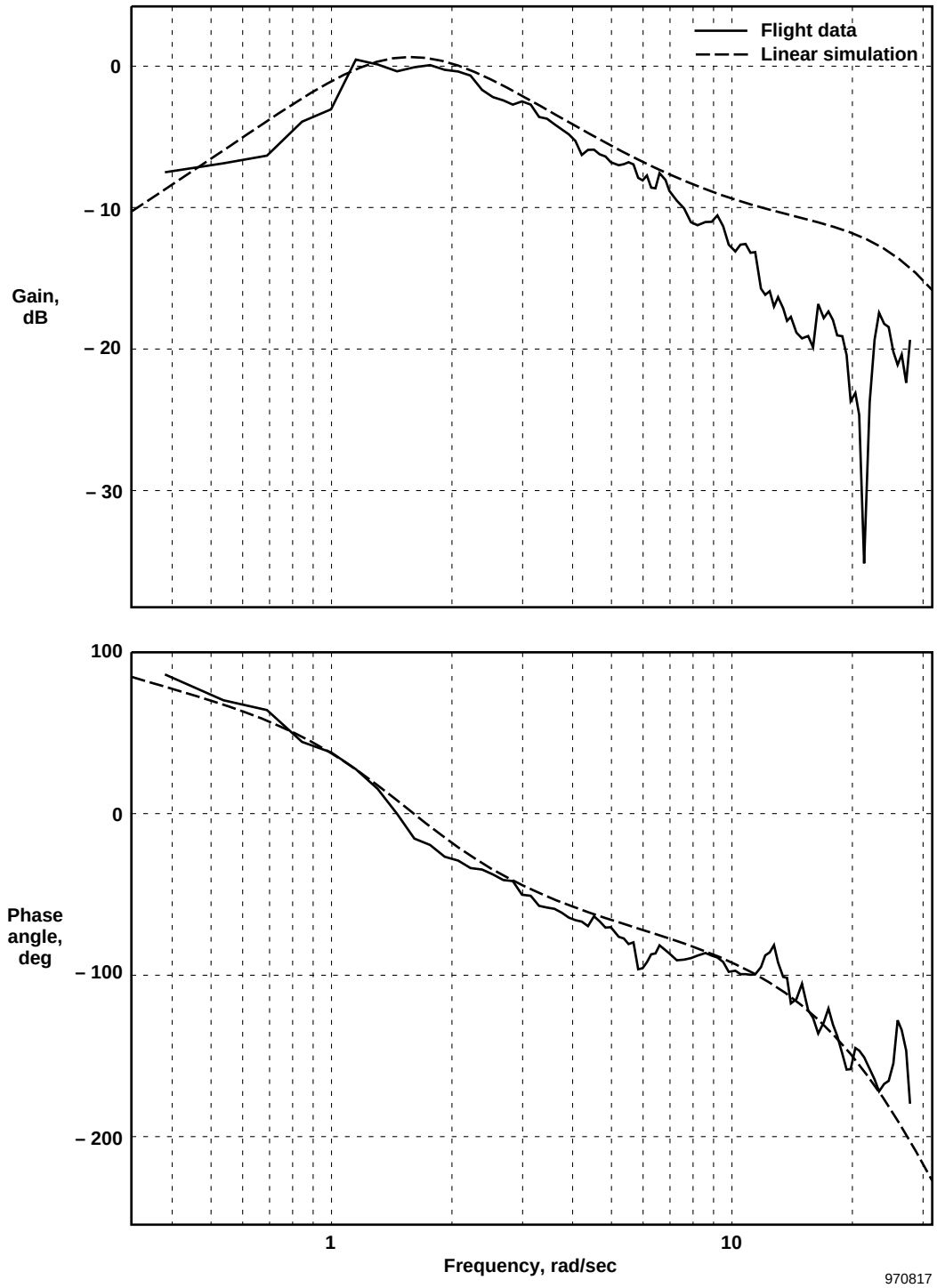

Figure 38. Frequency response comparison between linear simulation and flight data for *Q*/*ALFC* at 60° angle of attack.

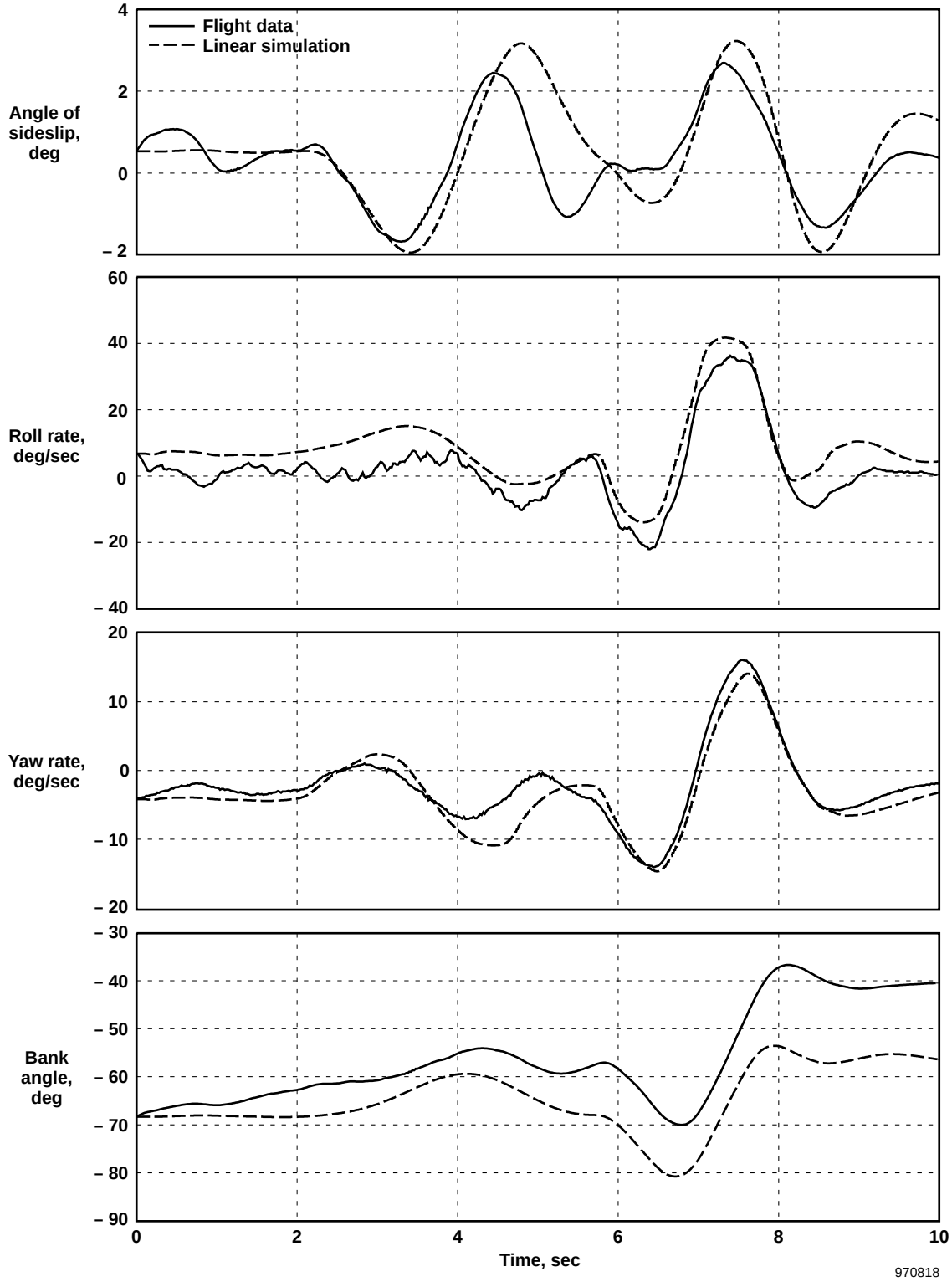

(a) Comparison of linear response with flight data for a roll doublet at 30° angle of attack.

Figure 39. Comparison between flight and simulation data at 30° angle of attack.

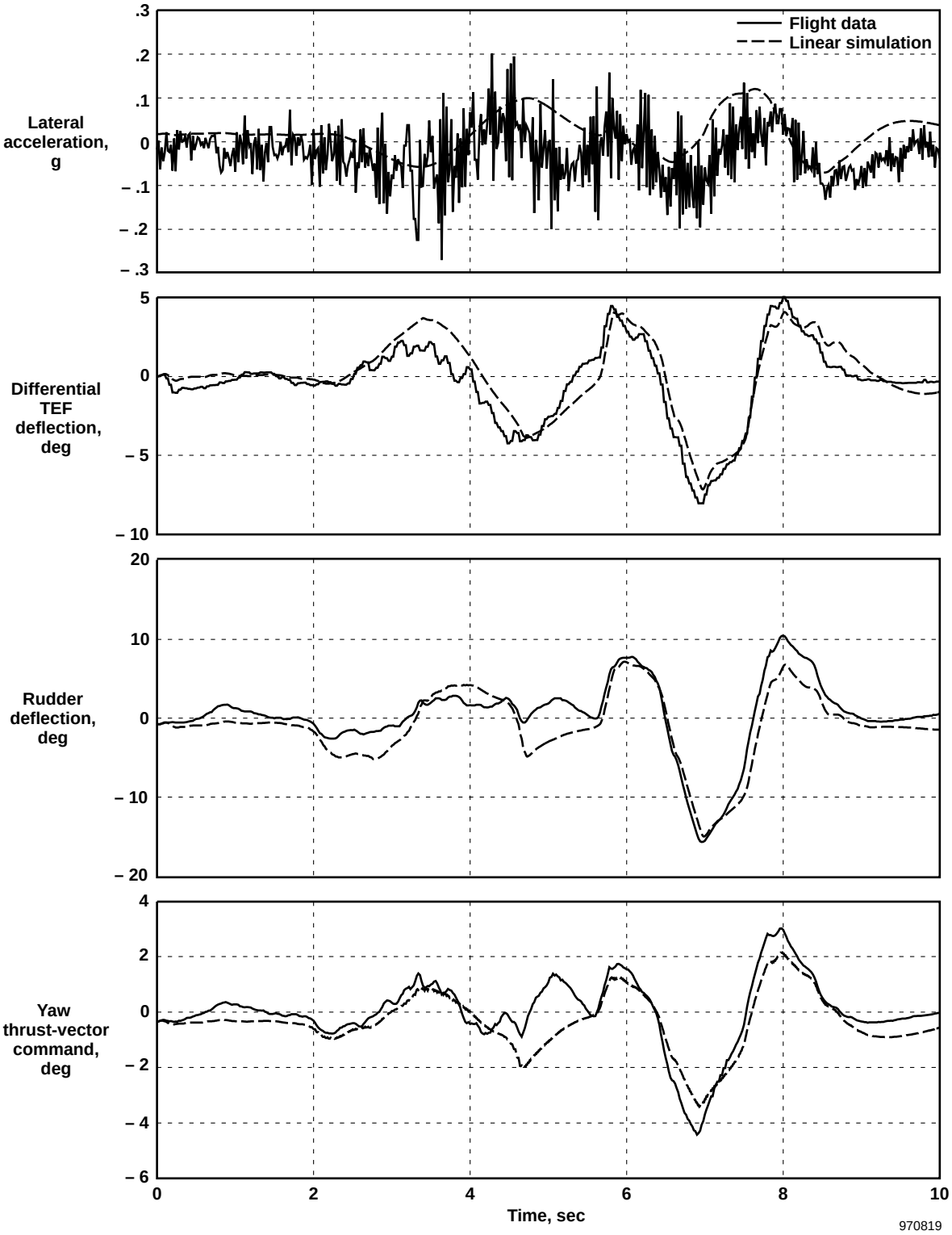

(b) Comparison of linear simulation response with flight data for a roll doublet at 30° angle of attack.

Figure 39. Continued.

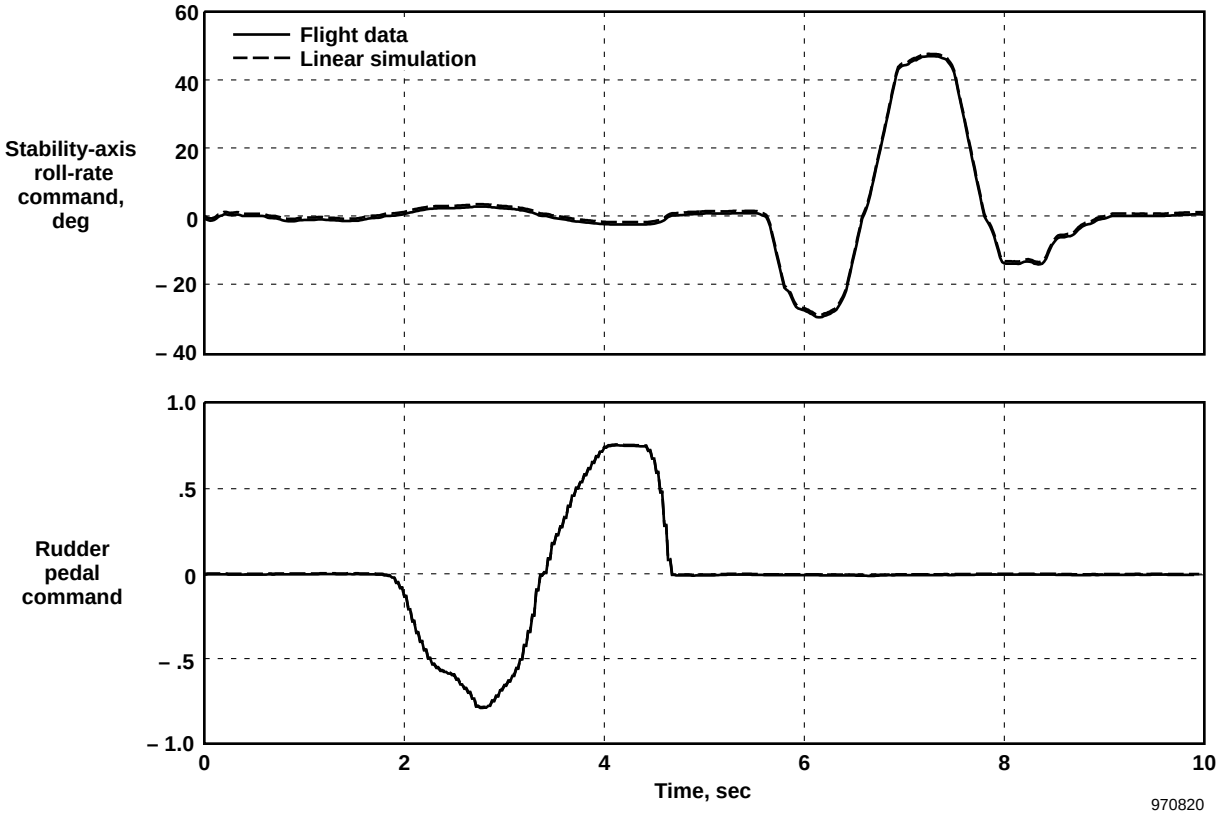

(c) Comparison of linear simulation response with flight data for a roll doublet at 30° angle of attack.

Figure 39. Concluded.

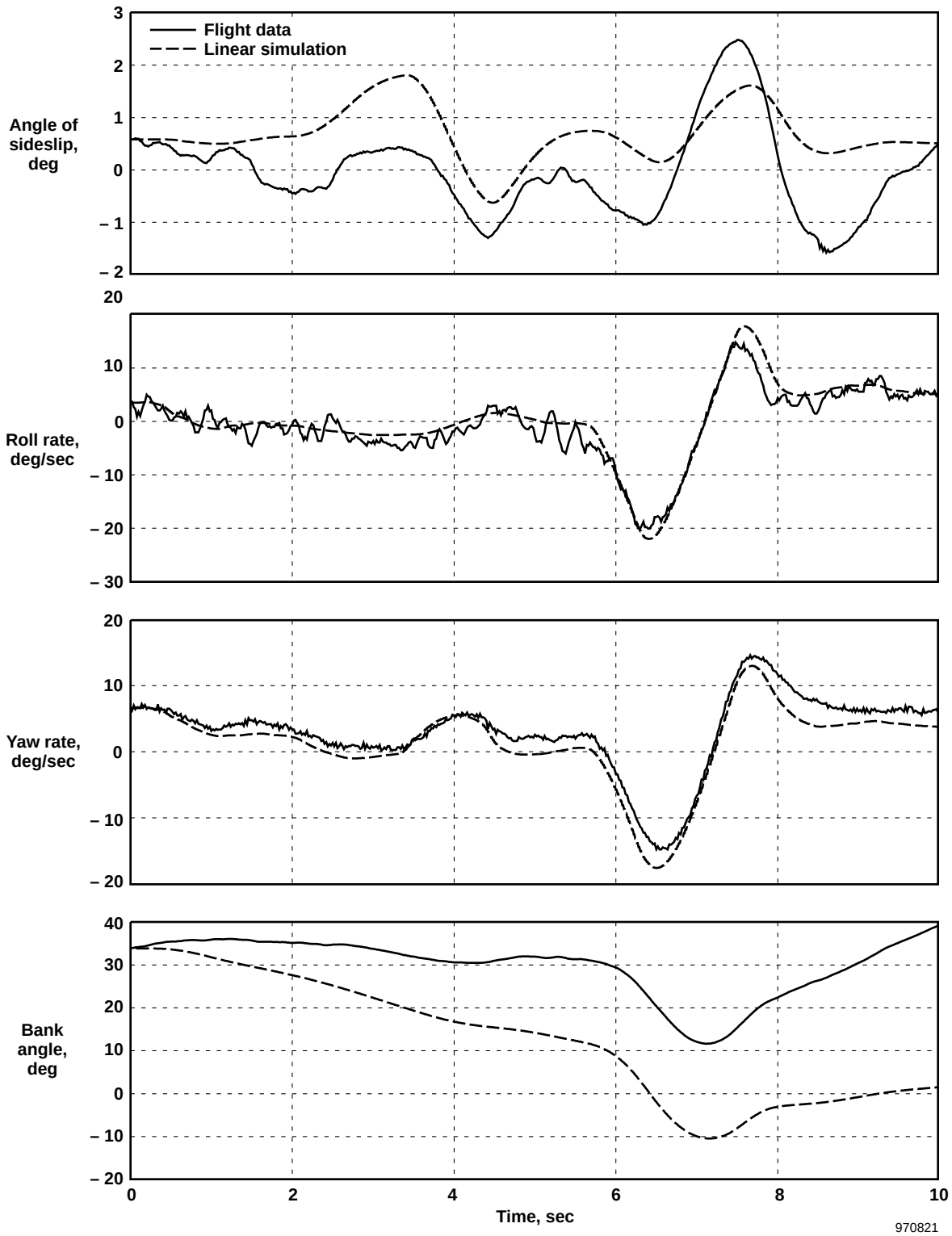

(a) Comparison of linear simulation response with flight data for a roll doublet at 45° angle of attack.

Figure 40. Comparison between flight and simulation data at 45° angle of attack.

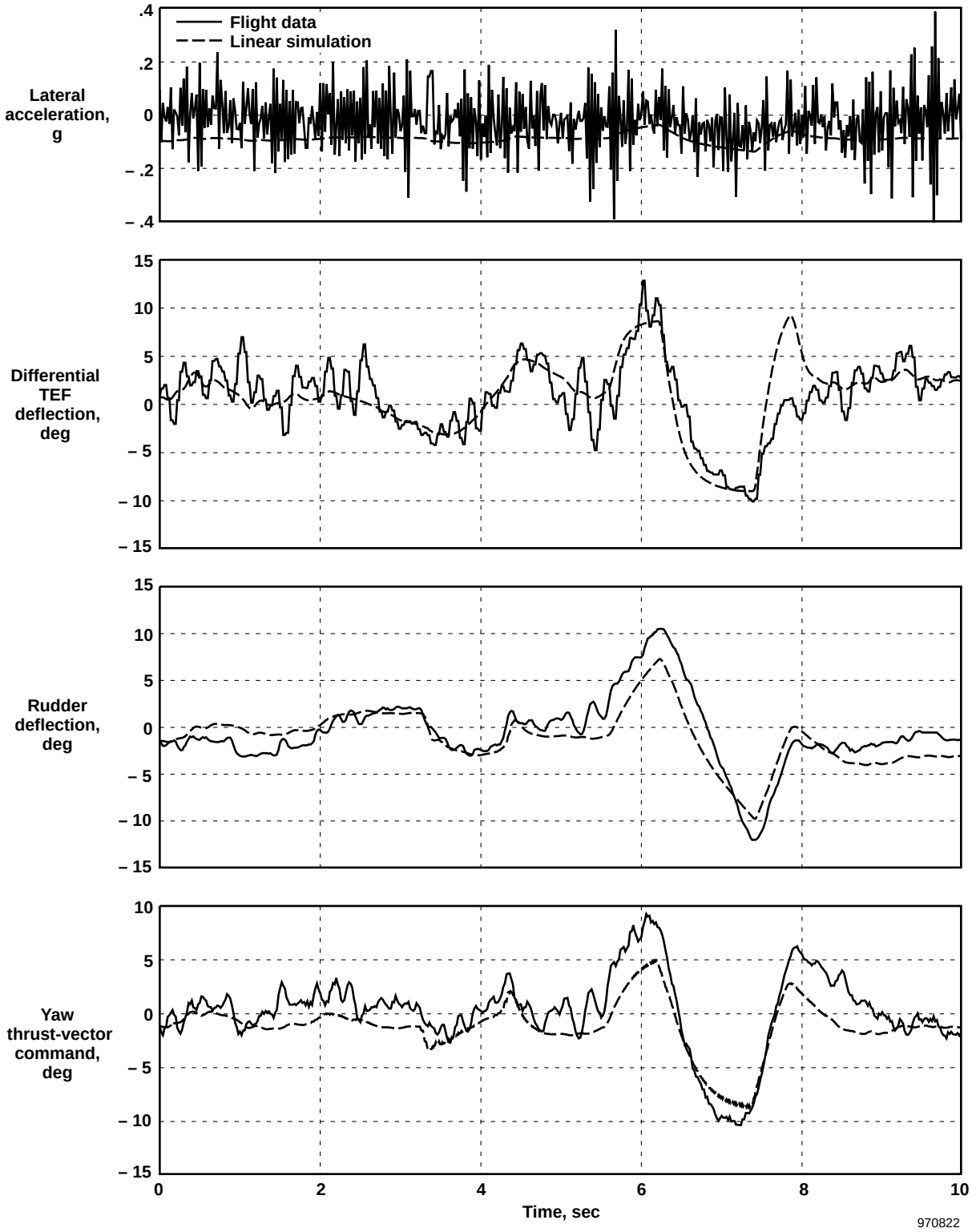

(b) Comparison of linear simulation response with flight data for a roll doublet at 45° angle of attack.

Figure 40. Continued.

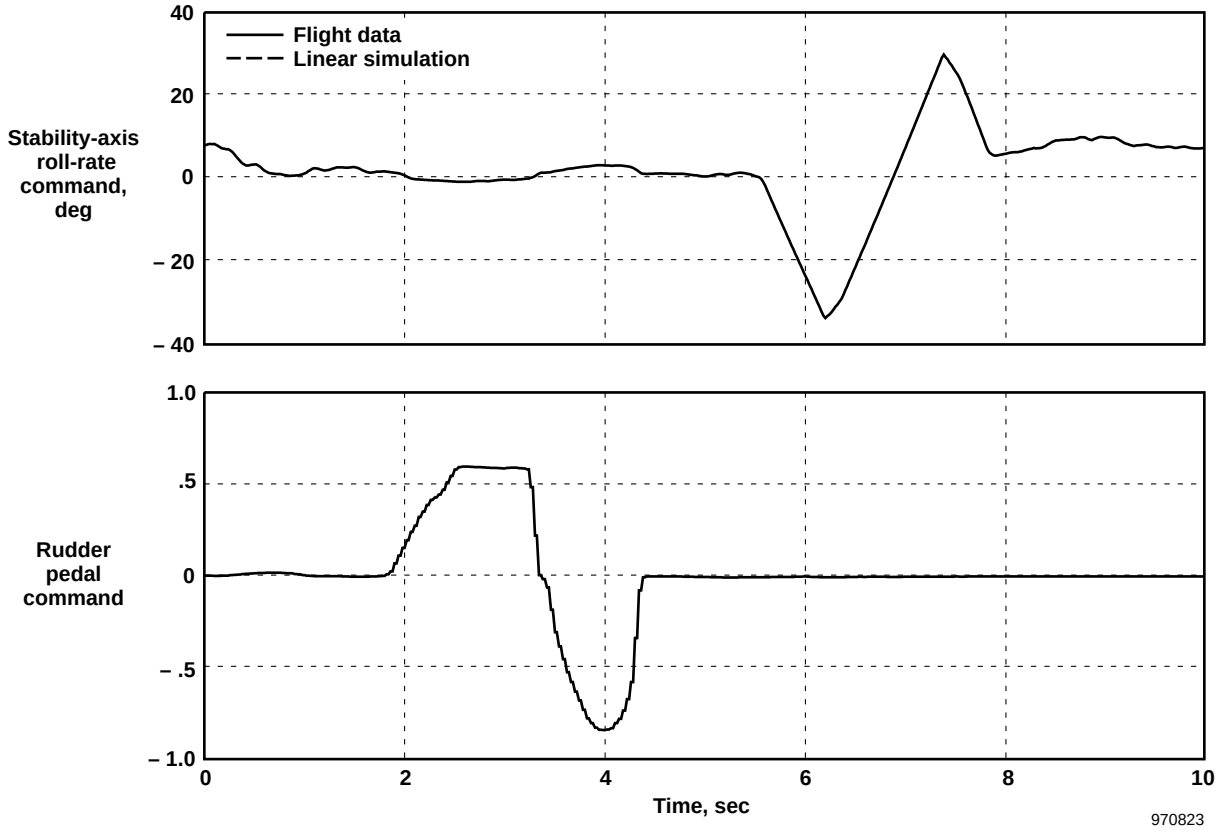

(c) Comparison of linear simulation response with flight data for a roll doublet at 45° angle of attack.

Figure 40. Concluded.

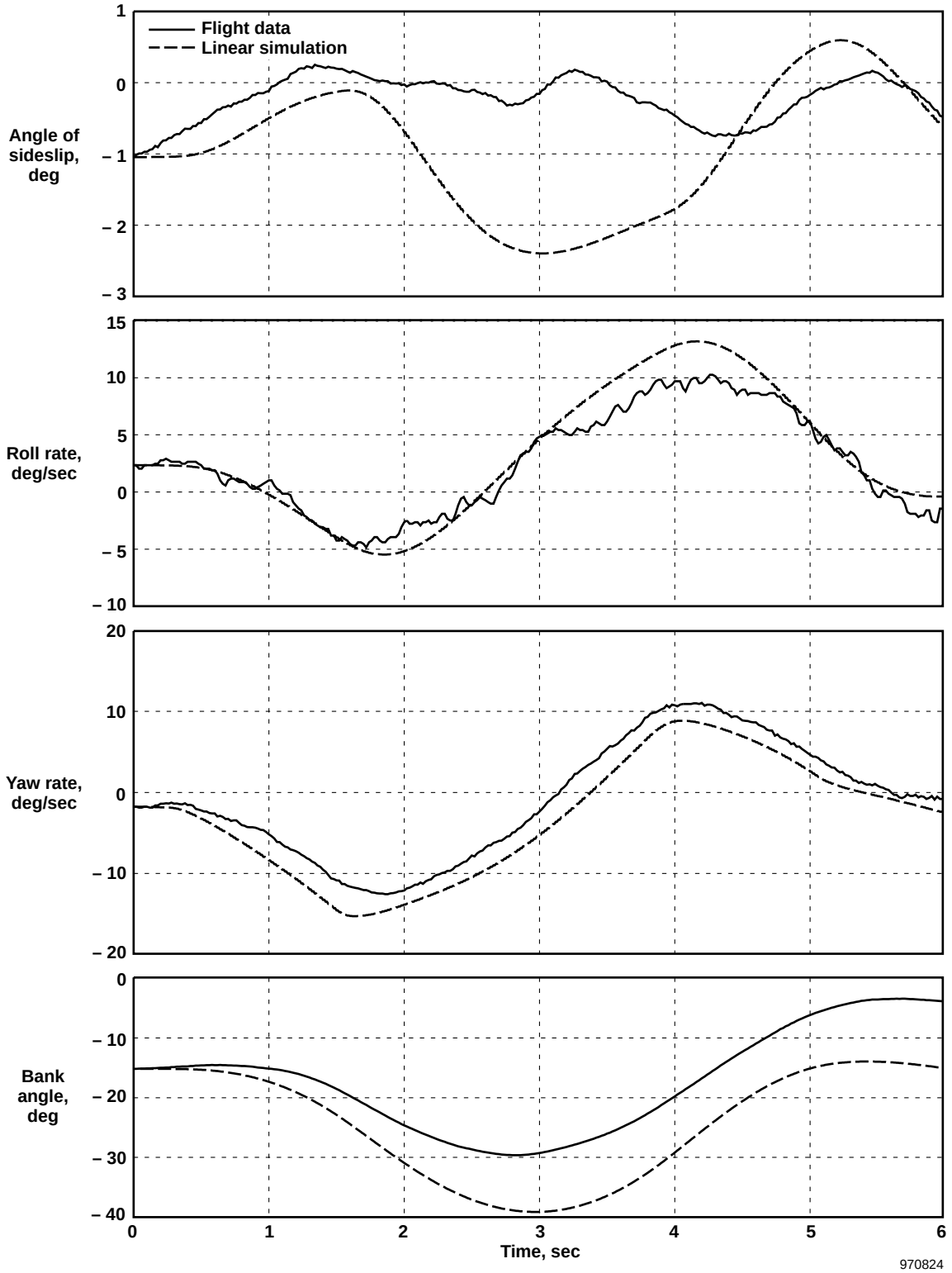

(a) Comparison of linear simulation response with flight data for a roll doublet at 60° angle of attack.

Figure 41. Comparison between flight and simulation data at 60° angle of attack.

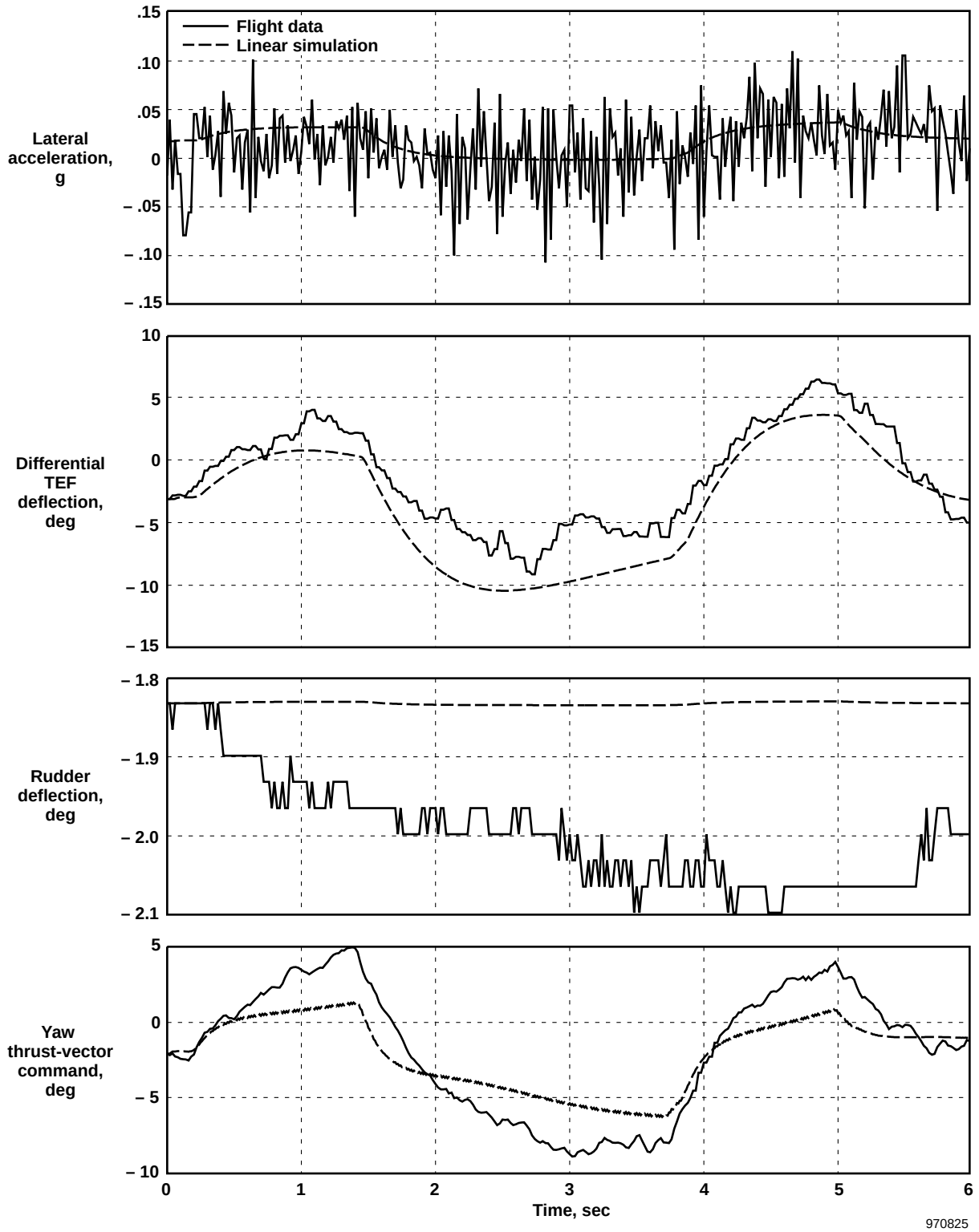

(b) Comparison of linear simulation response with flight data for a roll doublet at 60° angle of attack.

Figure 41. Continued.

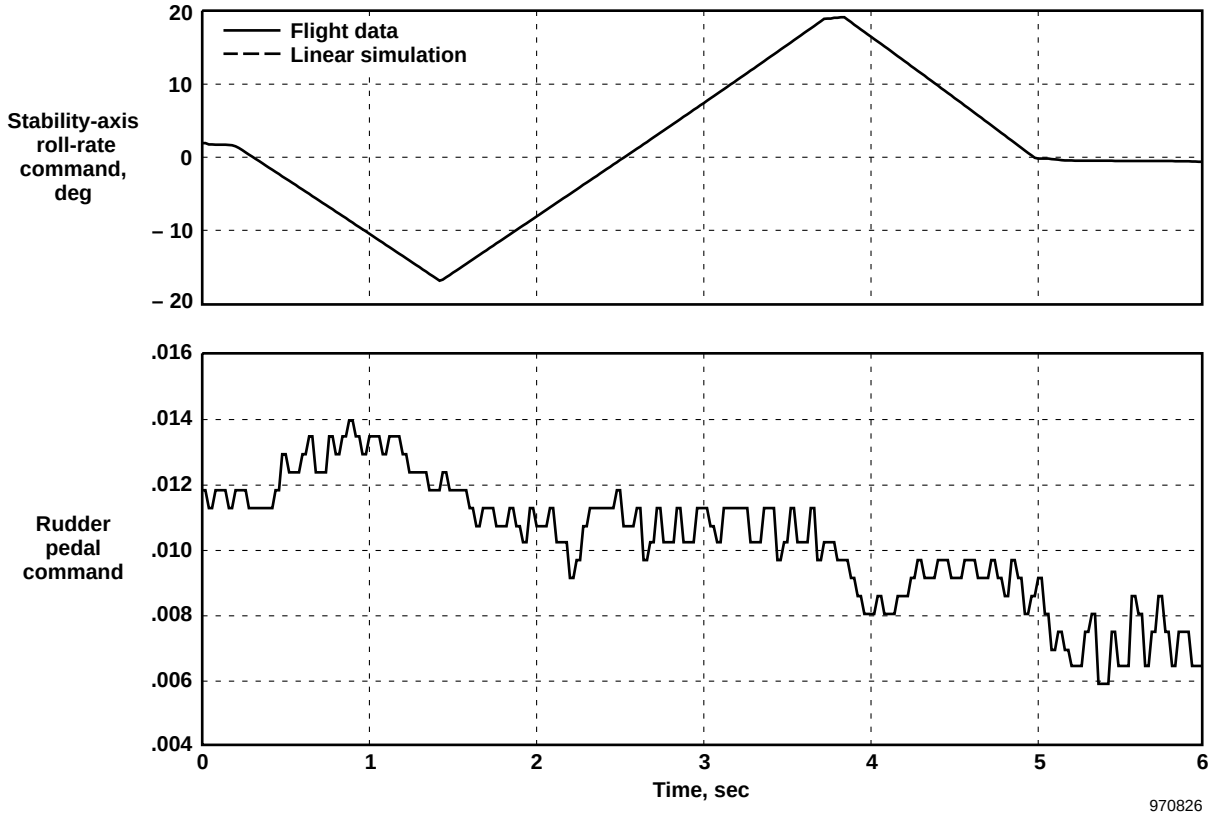

(c) Comparison of linear simulation response with flight data for a roll doublet at 60° angle of attack.

Figure 41. Concluded.

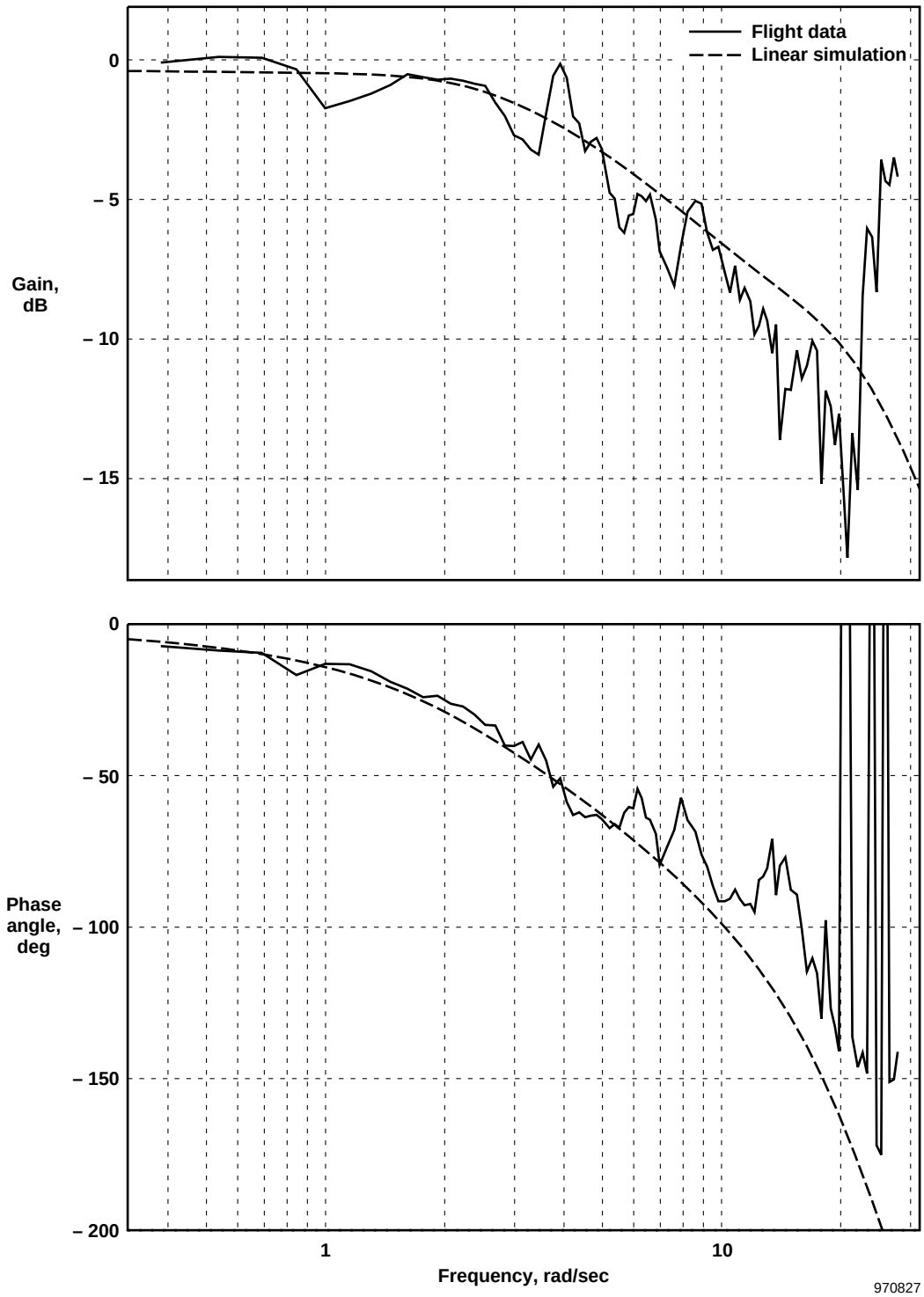

Figure 42. Frequency response comparison between linear simulation and flight data for *PSTAB*/*PKC* at 45° angle of attack.

REPORT DOCUMENTATION PAGE

Form Approved
OMB No. 0704-0188

Public reporting burden for this collection of information is estimated to average 1 hour per response, including the time for reviewing instructions, searching existing data sources, gathering and maintaining the data needed, and completing and reviewing the collection of information. Send comments regarding this burden estimate or any other aspect of this collection of information, including suggestions for reducing this burden, to Washington Headquarters Services, Directorate for Information Operations and Reports, 1215 Jefferson Davis Highway, Suite 1204, Arlington, VA 22202-4302, and to the Office of Management and Budget, Paperwork Reduction Project (0704-0188), Washington, DC 20503.

1. AGENCY USE ONLY (Leave blank)

2. REPORT DATE
December 1997

3. REPORT TYPE AND DATES COVERED
Technical Memorandum

4. TITLE AND SUBTITLE
Linearized Poststall Aerodynamic and Control Law Models of the X-31A Aircraft and Comparison with Flight Data

5. FUNDING NUMBERS
WU 529-30-04

6. AUTHOR(S)
Patrick C. Stoliker, John T. Bosworth, and Jennifer Georgie

7. PERFORMING ORGANIZATION NAME(S) AND ADDRESS(ES)
NASA Dryden Flight Research Center
P.O. Box 273
Edwards, California 93523-0273

8. PERFORMING ORGANIZATION REPORT NUMBER
H-2194

9. SPONSORING/MONITORING AGENCY NAME(S) AND ADDRESS(ES)
National Aeronautics and Space Administration
Washington, DC 20546-0001

10. SPONSORING/MONITORING AGENCY REPORT NUMBER
NASA/TM-97-206318

11. SUPPLEMENTARY NOTES

12a. DISTRIBUTION/AVAILABILITY STATEMENT
Unclassified—Unlimited
Subject Category 08

12b. DISTRIBUTION CODE

13. ABSTRACT (Maximum 200 words)

The X-31A aircraft has a unique configuration that uses thrust-vector vanes and aerodynamic control effectors to provide an operating envelope to a maximum 70° angle of attack, an inherently nonlinear portion of the flight envelope. This report presents linearized versions of the X-31A longitudinal and lateral-directional control systems, with aerodynamic models sufficient to evaluate characteristics in the poststall envelope at 30°, 45°, and 60° angle of attack. The models are presented with detail sufficient to allow the reader to reproduce the linear results or perform independent control studies. Comparisons between the responses of the linear models and flight data are presented in the time and frequency domains to demonstrate the strengths and weaknesses of the ability to predict high-angle-of-attack flight dynamics using linear models. The X-31A six-degree-of-freedom simulation contains a program that calculates linear perturbation models throughout the X-31A flight envelope. The models include aerodynamics and flight control system dynamics that are used for stability, controllability, and handling qualities analysis. The models presented in this report demonstrate the ability to provide reasonable linear representations in the poststall flight regime.

14. SUBJECT TERMS
Aircraft flight control system, Linear aerodynamics model, Rigid-body dynamic model, State space, X-31A airplane

15. NUMBER OF PAGES
67

16. PRICE CODE
A04

17. SECURITY CLASSIFICATION OF REPORT
Unclassified

18. SECURITY CLASSIFICATION OF THIS PAGE
Unclassified

19. SECURITY CLASSIFICATION OF ABSTRACT
Unclassified

20. LIMITATION OF ABSTRACT
Unlimited

NSN 7540-01-280-5500

Available from the NASA Center for AeroSpace Information, 800 Elkridge Landing Road, Linthicum Heights, MD 21090; (301)621-0390

Standard Form 298 (Rev. 2-89)
Prescribed by ANSI Std. Z39-18
298-102